

# Evaluating thermal losses and storage capacity in high-temperature aquifer thermal energy storage (HT-ATES) systems with well operating limits: insights from a study-case in the Greater Geneva Basin, Switzerland

M. Collignon<sup>1</sup>    Ø. S. Klemetsdal<sup>2,3</sup>    O. Møyner<sup>2,3</sup>    M. Alcanié<sup>1</sup>  
A. P. Rinaldi<sup>4</sup>    H. Nilsen<sup>3</sup>    M. Lupi<sup>1</sup>

1. Department of Earth Sciences, University of Geneva, Switzerland.
2. Norwegian University of Science and Technology, Trondheim, Norway.
3. SINTEF Digital, Oslo, Norway.
4. Swiss Seismological Service, ETH Zurich, Switzerland.

## Abstract

High-temperature aquifer thermal energy storage (HT-ATES) may play a key role in the development of sustainable energies and thereby in the overall reduction of CO<sub>2</sub> emission. To this end, a thorough understanding of the thermal losses associated with HT-ATES is crucial. We provide in this study a numerical investigation of the thermal performance of an HT-ATES system for a heterogeneous aquifer modelled after a well-defined region in the Greater Geneva Basin (Switzerland), where the excess heat produced by a nearby waste-to-energy plant is available for storage. We consider different aquifer properties and flow conditions, with complex injection strategies that respect maximum/minimum well pressures and temperatures, as well as legal regulations. Based on the results, we also draw conclusions on the economical feasibility (e.g., energy recovery factor vs. drilling costs) for the different strategies.

Our results indicate that the true behaviour of HT-ATES systems may deviate significantly from theoretical performance derived from idealised cases. This is particularly true when the operational pressure and temperature ranges of the wells are restricted, and for heterogeneous aquifers.

**keywords: Numerical Modelling; HT-ATES; Greater Geneva Basin**

# 1 Introduction

Global warming and pollution caused by industrial gas emissions and wastes urge for a rapid development of renewable energies and application of sustainable development policies (Colombo, 1992; Dincer, 1998; Hähnlein et al., 2013). A notable disadvantage of renewable and/or recycled energy compared to fossil fuels is the seasonal imbalance between the energetic demand and the production or availability of energy seen in regions of contrasted seasons (Dincer and Rosen, 2011). This results in an energy deficit and excess in winters and summers, respectively. Storing the excess of energy in the subsurface and exploit it later when needed, otherwise known as underground thermal energy storage (UTES), helps to buffer the seasonal imbalance and significantly contribute to reduce greenhouse gas emissions (Dincer, 2000; Andersson, 2007; Buscheck et al., 2017). Among the different UTES systems, aquifer thermal energy storage (ATES) is a cost-effective and suitable technology to store large amounts of energy, and has been increasingly used for heating and cooling of buildings (Bloemendal et al., 2014; Sommer et al., 2015; Schüppler et al., 2019). An ATES system stores sensible heat in an aquifer by injecting and withdrawing groundwater and often operates in a seasonal mode (Dickinson et al., 2009; Sommer et al., 2013). Cool groundwater is extracted through a cold well in summer to cool down buildings, while heated water is stored in the aquifer using a warm well at a different location. In wintertime the system is reversed: the heated water is extracted at the warm well to heat up buildings, while cool water is injected back into the aquifer at the cold well. Most of ATES systems store low-temperature groundwater (LT-ATES) in a range of 5 to 30°C (Drijver et al., 2012). High-temperature ATES (HT-ATES,  $T > 60^\circ\text{C}$ ) systems in contrast are limited due to legal aspects, often related to the restrictions on temperature increase during geothermal exploitation (Hähnlein et al., 2010; Drijver et al., 2012). Moreover, the first pilot studies reported increasing technical problems in wells (Jenne et al., 1992; Sanner, 1999) and a lower thermal recovery efficiency compared to LT-ATES systems (Molz et al., 1979, 1983a,b). Yet, HT-ATES systems possess a main advantage over LT-ATES systems since the stored energy can directly be used for heating purposes without the need for additional heat-pumps and are suitable for more applications (Drijver et al., 2012). Large amounts of heat from industrial residual waste, such as from incinerators and electricity plants, could then be stored in HT-ATES systems. These advantages combined with the rising energy prices and improvements in well and UTES technology (Van Lopik et al., 2016) have triggered a renewed interest in HT-ATES.

Besides legal regulations, one of the limiting aspects of HT-ATES are the thermal losses due to conduction and convection, which are aggravated with increasing injection temperatures. Previous studies established links between the thermal losses and the aquifer and injected water properties, or the aspect ratio of the volume of stored warm water (Hellström et al., 1979; Doughty et al., 1982; Bloemendal and Hartog, 2018). Free convection due to buoyancy forces during heat storage remains limited for low- to moderate-permeability aquifers (Hellström et al., 1979). However, low- to moderate-permeability aquifers

36 require adequate scaling of injection and production rates during the loading and unloading phases, re-  
37 spectively, to avoid rock fracturing and thus the loss of the entire heat stock. As a results, the volume  
38 of injected/produced warm water is smaller, or the loading/unloading phases need to be longer. There-  
39 fore, an appropriated balance between thermal losses and storage capacity needs to be evaluated when  
40 planning an HT-ATES system. The suitability of an ATES project is determined by its economical gain  
41 and compliance with legal regulations and thus requires a detailed characterisation of both the aquifer  
42 and aquiclude geology and physical properties, as well as the groundwater chemistry and flow character-  
43 istics (Andersson, 2007). Such assessments can be complex, and the use of numerical models has become  
44 a standard procedure in the evaluation and design optimisation of ATES projects. (O’Sullivan et al.,  
45 2000; Lee, 2010). Despite their complexity, many studies often consider equal and constant injected and  
46 produced volumes, and do not mention any scaling of rates as a function of pressure in the aquifer or  
47 permeability (Kim et al., 2010; Sommer et al., 2013, among others). Yet, it is important to consider more  
48 complex injection strategies to correctly evaluate the true stored volume and associated thermal losses,  
49 or thermal recovery, in particular in heterogeneous aquifers.

50 In this study, we investigate the competition between storage capacity and thermal losses for heteroge-  
51 neous aquifers in the Greater Geneva Basin (GGB), Switzerland. The Canton of Geneva, through the  
52 intermediate of the Services Industriels de Geneve (SIG), is currently interested in storing the excess  
53 of heat produced by the Cheneviers waste-to-energy plant in the suburban area of Geneva (Quiquerez,  
54 2017; HeatStore). In order to have a full control of the different parameters, we model here only the  
55 thermo-hydraulic behaviour of the HT-ATES system, without considering fluid-rock interactions and  
56 thermo-mechanical deformation. We investigate the thermal performances (i.e. storage and recovery)  
57 under different aquifer properties and injection schedules for the case of the Cheneviers plant, which  
58 results in different economical strategies. The aim is to define the conditions in the GGB that maximise  
59 the thermal recovery while complying with the local legal regulations and minimising the number of wells  
60 to be drilled. This study sets the basis for the ongoing energy storage effort in the GGB (and gener-  
61 ally in Switzerland and neighbouring countries) where similar heterogeneous aquifers are found in the  
62 North Alpine Foreland basin (PGG, 2011; GeoMolTeam, 2015). Finally, we also introduce a new open-  
63 access, user-friendly and efficient tool to investigate geothermal systems, with a support for complex well  
64 strategies.

## 65 2 The Greater Geneva Basin

### 66 2.1 Geological setting

67 The GGB forms the westernmost termination of the North Alpine Foreland Basin (also called Molasse  
68 Basin), located between France and Austria, parallel to the Alpine Orogen (Kuhlemann and Kempf,

69 2002). The GGB is bounded by the internal chain of the Jura Mountains to the northwest and by the  
 70 thrusting front of the Alpine units to the southeast (Fig 1a). The Variscan crystalline basement (*sensu*  
 71 *stricto*) of the GGB dips gently to the S-SE (1-3°) and is overlain by a thick (3000-5000 m) sedimentary  
 72 cover of Late Carboniferous to Quaternary deposits (Fig 1b). From the end of the Carboniferous through  
 73 Permian, SW-NE oriented grabens and relatively small confined basins formed in the basement. They  
 74 were later filled by continental clastic material, eroded from the Variscan orogen (Wilson et al., 2004;  
 75 McCann et al., 2006). These sediments and the crystalline basement form the basement *sensu lato* on  
 76 which the Triassic deposits unconformably rest (Signer and Gorin, 1995; Sommaruga, 1999). The Lower  
 77 Triassic (Buntsandstein) is formed of continental sandstones and is overlain by carbonates (Muschelkalk)  
 78 and evaporites (Keuper) that deposited in a shallow epicontinental sea (Diesler, 1914; Ramsay, 1963;  
 79 Trümpy, 1980). A rapid phase of marine transgression occurs during the Late Triassic (Rhaetian) and  
 80 Early Jurassic (Lias). The Lias sediments are mostly composed of bioclastic muddy limestones and dark  
 81 homogeneous marls that deposited in a distal marine environment (Fig 1b).

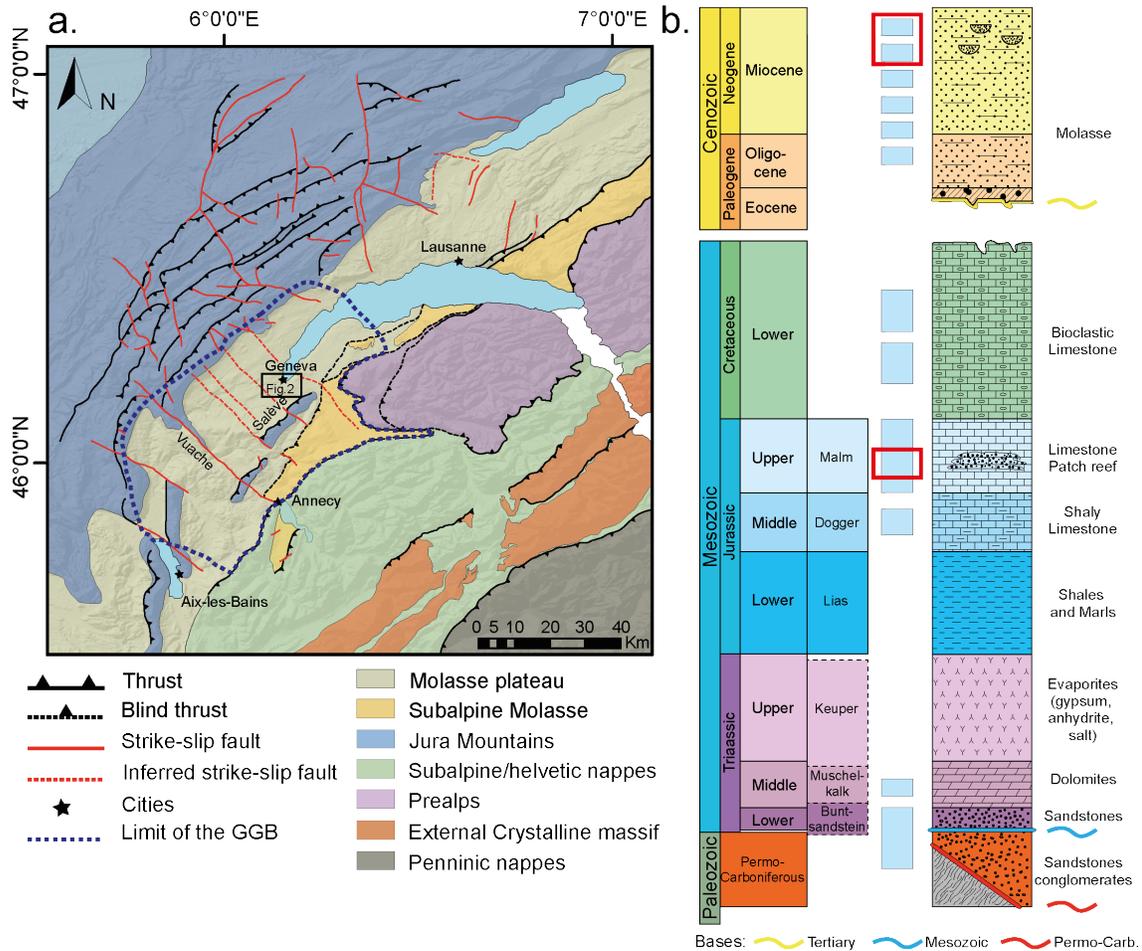


Figure 1: **a.** Simplified structural map of the Western Alps and Jura Mountains and **b.** Synthetic log and main aquifers of the Greater Geneva Basin. Red squares: aquifers investigated in this study. Modified after Chelle-Michou et al. (2017) and Chevalier et al. (2010).

82 Alternating marls and limestones deposited during the Dogger in a deep marine setting (Choffat, 1878;  
83 Conrad, 1969; Blondel, 1990). The Malm is characterised by shallower platform deposits evolving from  
84 marly and micritic limestones to biohermal reef facies (e.g. oolitic limestones, coral limestones and  
85 lagoonal limestones and calcarenites). The Lower Cretaceous is formed of fine grained bioclastic lime-  
86 stones that deposited in a shallow and warm marine environment (Charollais et al., 2013). During the  
87 Late Cretaceous, the GGB came to emersion and the Upper Cretaceous sediments, if deposited, were  
88 completely eroded, while the Lower Cretaceous units were largely karstified (Sommaruga, 1997). The  
89 warm and subequatorial climate of the Eocene accelerated the erosion of the latter, and the resulting red  
90 lateritic deposits filled the karsts and fractures (Becker et al., 2013; Hooker and Weidmann, 2007). The  
91 Mesozoic sequence is entirely covered in the basin by Oligocene to Late Miocene alpine sediments (i.e.  
92 Molasse) and Quaternary deposits but still outcrops locally in the Jura Mountains, the Mount Salève  
93 and the Mount Vuache (Charollais et al., 2007). The Molasse consists of marls and sandstones of marine  
94 and continental freshwater environments, whereas the Quaternary formations mostly have a glacial and  
95 fluvio-glacial origin (Amberger, 1978; Moscariello et al., 1998). The GGB is affected by two main sets of  
96 faults that accomodate the NW-SE alpine compression (Fig 1a). The first set consists of SW-NE thrusts  
97 in the Haute-Chaine of the Jura and in the subalpine Molasse, delineating the southeastern rim of the  
98 GGB (Fig 1) that are linked with the presence of reactivated Permo-Carboniferous lineaments (Signer  
99 and Gorin, 1995). The second set are strike-slip sinistral fault systems, mostly oriented NW-SE (e.g.  
100 Vuache fault) that laterally absorb the NW-SE shortening (Fig 1a). At depth, the Keuper evaporites  
101 act as a décollement level over which shortening of the Mesozoic and Cenozoic sedimentary cover is  
102 accommodated by SW-NE trending folds (Sommaruga, 1999).

103 Potential aquifers have been recognised in different stratigraphic units of the GGB (Rybach, 1992; Baujard  
104 et al., 2007; Chevalier et al., 2010), among which the freshwater Molasse sandstones and Malm patch reef  
105 carbonates represent promising targets for the development of ATEs systems.

## 106 **2.2 The Cheneviers waste-to-energy plant and district heating systems**

107 District heating systems consist in a network of underground pipes providing heat from a centralised  
108 plant, or from a number of distributed smaller heat production units, to a neighbourhood or a city  
109 (Fig. 2a). These systems play a key role in increasing the energy efficiency and reducing CO<sub>2</sub> emissions,  
110 by allowing the utilisation of heat from various sources, such as combined heat and power (CHP), heat  
111 from waste-to-energy plants and industrial wastes or geothermal and solar heat (Lund et al., 2014).  
112 The Canton of Geneva promotes the development of district heating systems, which currently represent  
113 less than 10% of the heating market (Quiquerez et al., 2016). These infrastructures comprise the large  
114 interconnected CADSIG and CADIOM city networks and recent smaller neighbourhood networks (e.g.  
115 Cartigny/Aire-la-ville) (Faessler et al., 2015). The CADSIG network, built in the 1960's, was initially

116 exclusively powered by gas boilers, whereas the CADIOM network was developed in the early 2000s  
 117 to recover the heat from the Cheneviers waste-to-energy plant (Fig. 2b). Their interconnection in 2012  
 118 allowed the transfer of heat from the CADIOM to CADSIG network and has increased the contribution of  
 119 waste heat into the network by 77 GWh (Quiquerez et al., 2015). Nevertheless, there is still every summer  
 120 an excess of 35 GWh from the Cheneviers plant (Fig. 2c) that could be optimised using seasonal ATEs  
 121 solutions (Quiquerez, 2017). This excess of energy is available in the form of a slightly over-pressured,  
 122 warm liquid water, at temperatures varying between 90 and 120°C (Faessler et al., 2015; Quiquerez,  
 123 2017).

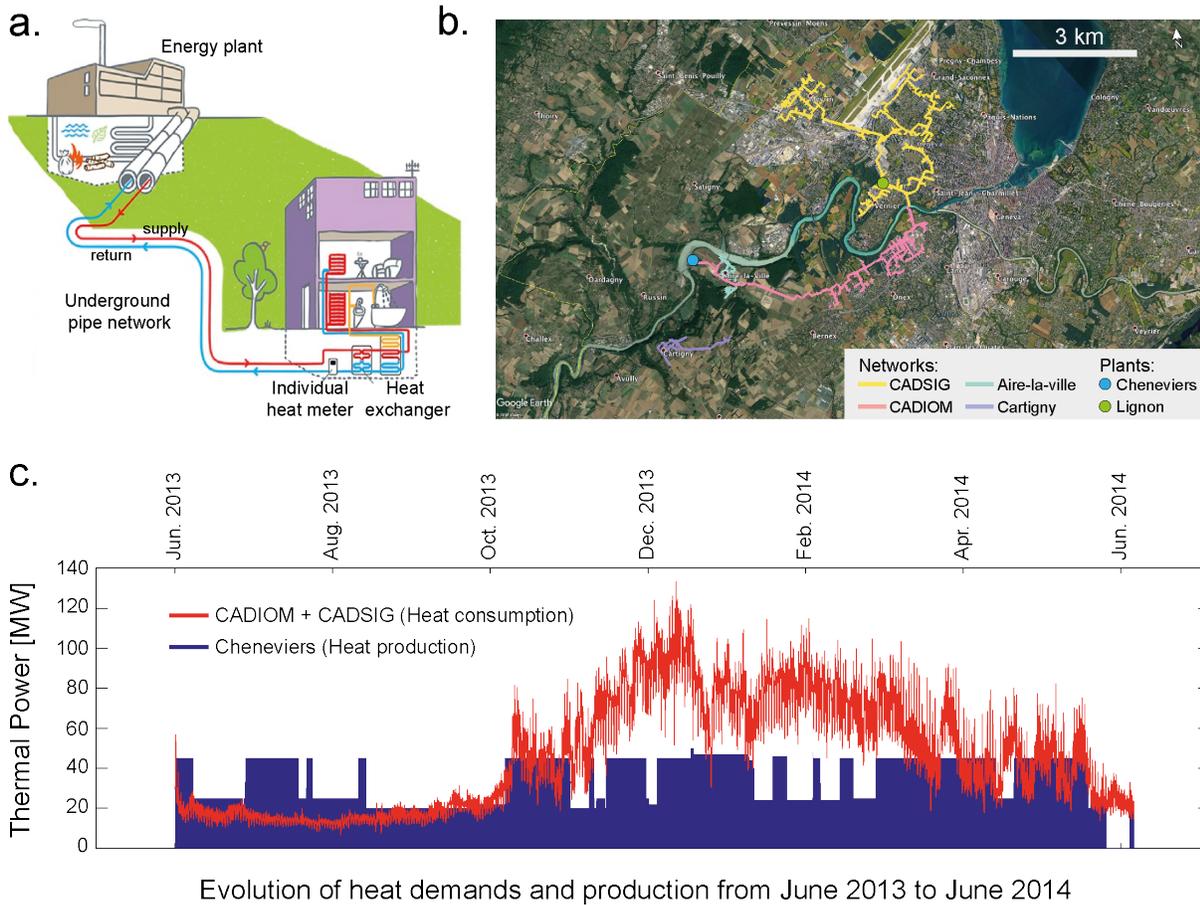


Figure 2: **a.** Schematic drawing showing the principle of a district heating system (source: SIG website, ww2.sig-ge.ch). **b.** Geographic distribution of the main networks and energy plants for district heating systems in the Geneva Canton. **c.** Evolution of heat demands from the CADSIG/CADIOM networks and heat production at the Cheneviers plant for the year 2013-2014. Modified after Quiquerez et al. (2016).

124 In this work, we numerically evaluate the possibility of storing this warm water in either the sandstone  
 125 channel bars of the Molasse deposits or in the patch-reef carbonates of the Malm units. These two  
 126 aquifers have very distinctive geometries and properties, and occur at different stratigraphic levels. The  
 127 shallow (< 1km) Molasse sandstones have a lateral extension ranging from ten to a few hundred metres

128 and show a moderate permeability (up to 1000 mD locally) and high porosity (up to 0.25), whereas the  
129 deep patch-reef carbonates have a fairly high porosity (0.15) but a low permeability (1-10 mD) (Platt  
130 and Keller, 1992; Chevalier et al., 2010; Rusillon, 2017). Rusillon (2017) recently provided a first review  
131 of the permeability and porosity measurements from well and outcrop samples in the GGB. The samples  
132 were measured in the laboratory using a gas porometer-permeameter. Rusillon (2017) also reported  
133 permeability and porosity derived from existing well logs (e.g. hydraulic tests). These measurements  
134 revealed a strong lateral and vertical heterogeneity of the rocks with permeability values showing two and  
135 four orders of magnitude difference for the Malm and Molasse units, respectively. We therefore perform  
136 a parametric study with homogeneous properties for each aquifer type (i.e. Molasse or Malm) that we  
137 present in the results. The economical applications and limitations of this study are then discussed, along  
138 with additional supporting simulations.

## 139 3 Model

### 140 3.1 Model presentation

141 Numerical simulations of an HT-ATES exploitation can be performed with any groundwater flow mod-  
142 elling software that also considers heat transfers. Among these, COMSOL, ANSYS FLUENT, UTMECH,  
143 SEAWAT (MODFLOW family), FEFLOW and TOUGH2 are the most commonly used (Lee, 2010; Din-  
144 cer and Rosen, 2011). Two aspects are particularly important for simulations of HT-ATES. The first is  
145 that a variable density and viscosity should be implemented to capture buoyancy forces, resulting from a  
146 density contrast between the injected and the ambient water (Doughty et al., 1982). The second aspect is  
147 the possibility of having a mesh refinement around specific parts in the model. This is not mandatory but  
148 rather convenient for computing performance, since high spatial resolution is typically only needed near  
149 wells. For this study, we use the MATLAB Reservoir Simulation Toolbox (MRST), which is an open-  
150 source code compatible with both proprietary (MATLAB) and open source (Octave) software aiming at  
151 rapid prototyping of new models and solution strategies for flow in porous media (Krogstad et al., 2015;  
152 Lie et al., 2012; Lie, 2019). The toolbox consists of several modules, with support for complex fluid physics  
153 and well scheduling, as well as flexible meshing capabilities, but has until now lacked proper support for  
154 geothermal simulations. We have developed a new geothermal module in MRST (called *geothermal*) to  
155 investigate heat and mass transport in the GGB. MRST is designed to have the entire workflow within a  
156 single framework, from direct import of geophysical and geological data to fluid flow modelling. Moreover,  
157 it provides full control over every aspects of the implementation, including fluid and rock properties, well  
158 trajectories and injection strategies, as well as numerical considerations such as meshing, discretisations,  
159 linear/nonlinear solvers, etc. The support of the existing generic algorithms and their flexibility was a  
160 motivation to implement a new geothermal module in MRST. A key distinguishing feature of MRST as a

161 prototyping tool is the use of automatic differentiation, where no manual implementation of Jacobians or  
 162 linearised systems are required. Implementing new governing equations is as simple as implementing the  
 163 discrete residual with the standard differential operators already implemented in MRST, and Jacobians  
 164 and a nonlinear solver is automatically defined for the user. As the implementation of Jacobians for new  
 165 functions can be a time-intensive part of the development process, we believe this greatly improves both  
 166 prototyping speed and robustness of the resulting simulator.

The newly developed module *geothermal* implements a non-isothermal single-phase, two-component model for flow in porous media to simulate the injection/production of liquid water in an aquifer. The model equations describe conservation of total fluid mass (i.e. pure water or brine) and concentration of sodium chloride (NaCl), as well as conservation of energy. The two mass-conservation equations read

$$\frac{\partial}{\partial t}(\phi\rho_f) + \nabla \cdot (\rho_f\vec{v}) = q_f, \quad (1)$$

$$\frac{\partial}{\partial t}(\phi c\rho_f) + \nabla \cdot (c\rho_f\vec{v}) + \nabla \cdot (\phi\tau\rho_f D\nabla c) = q_b, \quad (2)$$

167 where  $\phi$  is the porosity,  $\rho_f$  the fluid density,  $c$  the mass fraction of NaCl,  $\tau$  the tortuosity of the medium  
 168 and  $D$  the NaCl molecular diffusivity. The Darcy velocity  $\vec{v}$  is given from Darcy's law:

$$\vec{v} = -\frac{1}{\mu_f}\mathbf{K}(\nabla p - \rho_f g\nabla z), \quad (3)$$

169 where  $\mathbf{K}$  is the permeability tensor,  $\mu_f$  the fluid viscosity,  $z$  the depth and  $g$  the gravity acceleration.  
 170 Moreover,  $q_f$  and  $q_b$  denote source/sink terms (e.g. wells) for total fluid and NaCl, respectively. Finally,  
 171 conservation of energy in the system is given by

$$\frac{\partial}{\partial t}((1-\phi)\rho_r C_r T + \phi\rho_f u_f) + \nabla \cdot (\rho_f h_f \vec{v}) - \nabla \cdot \lambda \nabla T = q_T, \quad (4)$$

172 with  $\rho_r$  and  $C_r$  the density and heat capacity of the rock, respectively, and  $u_f$  and  $h_f$  are the internal  
 173 energy and enthalpy of the fluid. The temperature is denoted by  $T$ , and the thermal conductivity  $\lambda$  is  
 174 defined by

$$\lambda = \phi\lambda_f + (1-\phi)\lambda_r, \quad (5)$$

175 where  $\lambda_r$  and  $\lambda_f$  are the conductivity of the rock and fluid, respectively. Injected/produced energy is  
 176 denoted  $q_T$ . The density and viscosity of the fluid are calculated as a function of pressure, temperature  
 177 and NaCl concentration using the formulation of Spivey et al. (2004) that has already been implemented  
 178 in MATLAB (Collignon et al., 2018a,b). This formulation is valid under the ranges of investigated tem-  
 179 perature, pressure and NaCl concentration in our study. Table 1 summarises the parameters used herein.  
 180 We solve equations (1) – (4) numerically using a fully implicit finite-volume discretisation with two-point  
 181 flux approximation and single-point upstream mobility weighting. This gives a robust discretisation that  
 182 is stable over a wide range of timesteps (Lie, 2019; Lie et al., 2012; Krogstad et al., 2015).

183 A comparison of *geothermal* with the commercial flow simulator TOUGH2 (Pruess et al., 1999) yields less  
 184 than 2% difference in the results. This small discrepancy can be explained by the different implementation

185 of fluid properties in both codes (see suppl. mat.). In addition to this benchmark, comparisons with  
186 analytical solutions and simple conservative tests have been performed to ensure the correctness of our  
187 numerical implementation. Our tests show that *geothermal* captures the main physical processes at play  
188 during HT-ATES exploitation (suppl. mat.).

Symbol	Unit	Definition	Value range
$x, y, z$	m	coordinates	–
$L_x, L_y, L_z$	m	initial dimensions of the model in $x, y$ and $z$ directions	800, 500, 310–450
$h_{\text{top}}$	m	top layer thickness	0–50
$h_{\text{aq}}$	m	aquifer thickness	10–150
$d_{\text{aq}}$	m	aquifer depth	150–1500
$k$	mD	aquifer permeability	0.001–500
$\phi$	–	aquifer porosity	0.01–0.3
$\vec{v}$	m s <sup>-1</sup>	Darcy velocity	–
$v_{\text{aq}}$	m a <sup>-1</sup>	aquifer flow velocity	0–50
$c$	–	NaCl mass fraction	0.002–0.06
$C_r$	J kg <sup>-1</sup> K <sup>-1</sup>	rock heat capacity	2300
$C_f$	J kg <sup>-1</sup> K <sup>-1</sup>	fluid heat capacity	4200
$C_{\text{aq}}$	J kg <sup>-1</sup> K <sup>-1</sup>	aquifer heat capacity	–
$\lambda_r$	W m <sup>-1</sup> K <sup>-1</sup>	rock thermal conductivity	1.8
$\lambda_f$	W m <sup>-1</sup> K <sup>-1</sup>	fluid thermal conductivity	0.6
$\lambda_{\text{aq}}$	W m <sup>-1</sup> K <sup>-1</sup>	aquifer thermal conductivity	–
$\rho_r$	kg m <sup>-3</sup>	rock density	2500
$D$	m <sup>2</sup> s <sup>-1</sup>	NaCl molecular diffusivity	10 <sup>-6</sup>
$\tau$	–	medium tortuosity	1
$\mu_f$	Pa s	fluid viscosity	–
$\rho_f$	kg m <sup>-3</sup>	fluid density	–
$V_f$	m <sup>3</sup>	injected fluid volume	–
$E$	J	energy	–
$P$	W	thermal power	–
$\eta$	–	energy recovery factor	–
$T_{\text{cold}}$	°C	temperature of injected water at the cold well	12.61 – 49.9
$T_{\text{warm}}$	°C	temperature of injected water at the warm well	60 – 120
$T_{\text{lim}}$	°C	cut-off temperature for the unloading phase	none – 100
$bhp_{\text{min}}$	bar	minimum well pressure	1
$bhp_{\text{max}}$	bar	maximum well pressure	75 – 250
$Q_{\text{inj}}$	L s <sup>-1</sup>	injection rate	5 – 20
$Q_{\text{prod}}$	L s <sup>-1</sup>	production rate	5 – 20

**Table 1:** Physical parameters for the study. Only the values (or range) of input parameters are reported in the 4<sup>th</sup> column. Values (or range) calculated by the model such as density, viscosity, pressure and temperature are not reported here.

### 189 3.2 Geometry, boundary conditions and key assumptions

190 Our aim is to understand the primary control of rock properties and aquifer flow conditions on the thermal  
 191 performance and environmental impact of a HT-ATES system. Therefore, we employ a simple model  
 192 geometry as more complex geological surfaces could induce preferential flow directions that would bias  
 193 the interpretation of the parameter controls. The generic model consists in a 3D block with a lateral area  
 194 of  $800 \times 500 \text{ m}^2$ , and a vertical thickness that varies between 310 and 450 m for different configurations  
 195 (Fig. 3a)

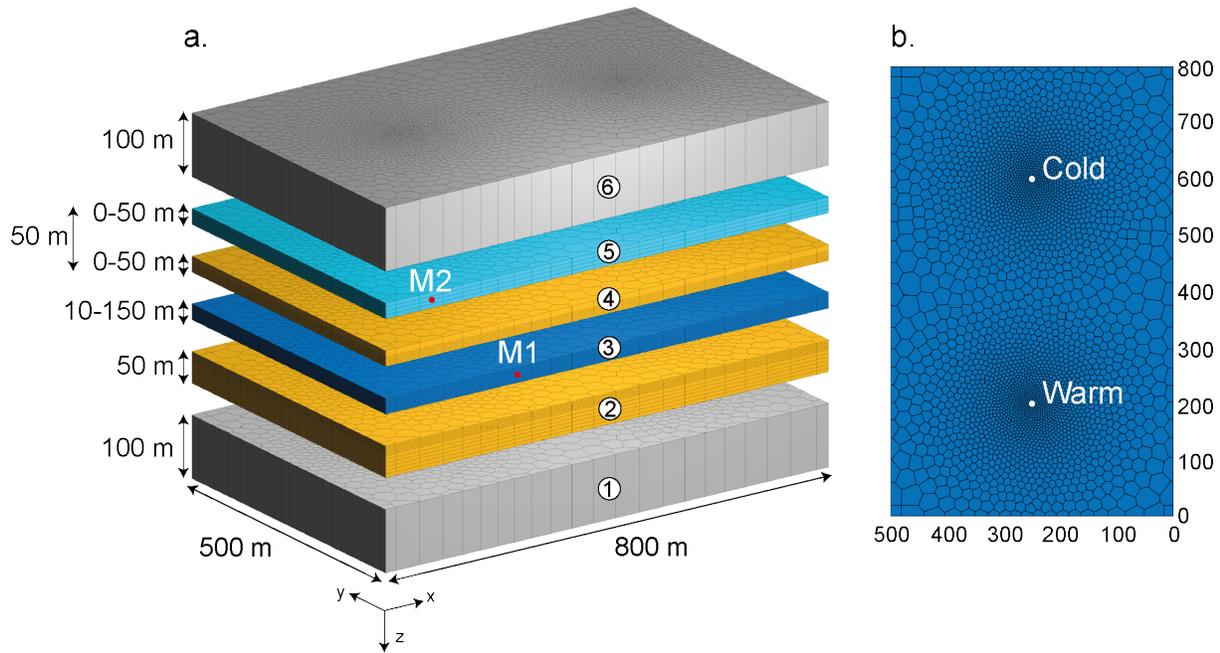


Figure 3: **a.** Side-view of the generic model (decomposed) with layer dimensions. Not to scale. Grey: low permeable pad layers (1 and 6), dark blue: storage aquifer (3), light blue: drinking water aquifer (5), yellow: low-permeability rock layers (2 and 4). **b.** Top view of the aquifer with well location and mesh resolution. M1-M2: monitoring points used to evaluate the HT-ATES environmental impact, projected on the front side of the model (see Fig. 9).

196 The model is divided into different layers (1-6 in Fig. 3a) with from bottom to top: a 100 m low permeable  
 197 padding layer (1), a 50 m low permeable rock (2), a 10-50 m storage aquifer (3), a 0-50 m low permeable  
 198 rock (4), a 0-50 m shallower aquifer (5) and a 100 m low permeable padding layer (6). Layers 4 and 5  
 199 always have a total thickness of 50 m (Fig. 3). In addition to the thickness of the storage aquifer (3), we  
 200 also vary the thickness of its upper low-permeability unit (4) to investigate the effect of heat storage on  
 201 an overlying aquifer of drinking water (5). Such a configuration can be found in the GGB, with drinking  
 202 water aquifers occurring in Quaternary deposits (GeoMolTeam, 2015). The padding layers (1,6) are used  
 203 to prescribe boundary conditions away from the aquifer, so that they reflect a basin equilibrium state  
 204 and do not perturb the flow field induced by injection and extraction of water at the wells.

205 We generate the unstructured grid with the *upr* module (Berge et al., 2018) to allow a mesh refinement

206 around specific areas inside the model (e.g. wells, aquifers, aquifer-rock interfaces), where pressure and  
 207 temperature variations can be sharp. The mesh is radially refined around the wells, with a finest horizontal  
 208 resolution of 2 m (Fig. 3b). The storage aquifer (3) has a vertical resolution of 2 m. The low-permeability  
 209 rock units (2,4) and/or shallower aquifer (5) have a vertical resolution of 2 m in the first 30 m, near the  
 210 aquifer, and of 5 m for the rest of these units. Finally, the padding layers (1,6) only have two elements  
 211 in the vertical direction (Fig. 3a). Additional tests (not reported here) have shown that this resolution  
 212 is sufficient as mass and heat transfers in this part of the model are negligible.

213 We consider an HT-ATES system with a pair of wells, called "warm" and "cold", that operate in an  
 214 opposite mode. When the cold well is injecting, the warm well is producing and vice-versa. Similar  
 215 to LT-ATES systems used in heating/cooling of buildings, each well operates successively in injection  
 216 and production modes, depending of the season. We therefore refer to warm/cold rather than injec-  
 217 tion/production wells, as warm (or cold) water is always injected (or produced) at the same well. The  
 218 thermal radius ( $R_{th}$ ) of an ATES well corresponds to the maximum distance from the injection well  
 219 reached by the thermal front in a homogeneous medium (Sommer et al., 2015; Bloemendal et al., 2018).  
 220 It serves as an initial estimate of the thermally affected area around the well and is defined as

$$R_{th} = \sqrt{\frac{C_f V_f}{C_{aq} \pi h_{aq}}}, \quad (6)$$

221 where  $C_{aq}$  and  $C_f$  are the aquifer and fluid heat capacity, respectively,  $V_f$  the volume of injected fluid, and  
 222  $h_{aq}$  the aquifer thickness. To do a clean-cut comparison between the different investigated configurations,  
 223 we keep a constant distance between the wells in all simulations. This distance is 400 m and corresponds  
 224 to twice the maximum estimated thermal radius, as recommended by Sommer et al. (2013) to limit  
 225 thermal interference. This maximal thermal radius is estimated for the simulation with the minimal  
 226 aquifer thickness and maximal injected volume.

227 We assume an initial quasi-hydrostatic pressure gradient in the entire model (defined as  $p_0 = \rho g z$ , with  
 228  $\rho = 1000 \text{ kg m}^{-3}$ ). The temperature gradient in the GGB varies with depth (Chelle-Michou et al.,  
 229 2017). Accordingly, we prescribe a temperature gradient of 17.4 and 26.6°C/km for the Molasse and  
 230 Malm aquifers, respectively, and a surface temperature of 10°C. Equilibrium pressure and temperature  
 231 conditions (similar to initial gradients) are imposed at all boundaries. We specify a flux boundary  
 232 condition on the back-side of the model (faces parallel to the  $x$ -axis, at  $y = 500 \text{ m}$ ) when investigating  
 233 the effects of the aquifer flow velocity. This boundary condition is only assigned to the back-side faces of  
 234 the storage aquifer (layer 3, Fig. 3).

235 The estimated lifetime of an ATES system ranges from 25 to 50 years (Hartog et al., 2013; Bloemendal  
 236 et al., 2014) and its payback time (i.e. time before it is economically viable) typically varies between 2 and  
 237 10 years, but can be up to 15 years (Fleuchaus et al., 2018). To ensure that we reach the payback time and  
 238 the maximum thermal recovery in our study, we simulate the HT-ATES exploitation for 20 years, which

239 corresponds to 20 repeating cycles. We use the same exploitation schedule for the wells in all simulations.  
240 A cycle is divided into an equal loading and unloading phase of four months, separated by two months of  
241 rest. The loading phase corresponds to the storage of warm water in the aquifer (from May to August,  
242 Fig. 2c), whereas the unloading phase is its withdrawal from the aquifer (from November to February).  
243 No water is neither injected nor extracted during the resting phases. In the following parametric study,  
244 we set the temperature of the injected water at the warm well to 90°C, which corresponds to the supply  
245 temperature of the CADSIG/CADIOM networks during summer (Faessler et al., 2015; Quiquerez et al.,  
246 2015). The temperature of the injected water at the cold well varies between 12.6 and 49.9°C, depending  
247 on the model configuration, and is equivalent to the initial temperature at the top of the aquifer. Injection  
248 and production rates are set identical to keep a pressure balance in the aquifer and to ensure that the  
249 volume of injected or pumped water complies with legal recommendations (CH-GSchV, 1998; OFEV,  
250 2009). The rates vary between 5 and 20 L s<sup>-1</sup>, depending on the aquifer permeability and depth. Lower  
251 and upper limits of the bottom hole pressure (bhp) at the wells are imposed to ensure that the pressure  
252 does not drop below unrealistic values (< 1 bar) or does not exceed a failure criteria (e.g. lithostatic  
253 pressure). A cut-off based on temperature can also be used during the unloading phase depending on  
254 the desired application of the stored energy: once the temperature drops below this cut-off limit, both  
255 wells stop injecting and producing and the remaining time of the unloading phase becomes a resting  
256 phase.

### 257 3.3 Choice of aquifers and well parameters

258 Although many studies focus on the GGB, some physical parameters such as the aquifer flow velocity and  
259 salinity, as well as the thermal rock properties remain poorly constrained (Rusillon, 2017; GeoMolTeam,  
260 2015). Permeability and porosity measurements reveal a strong heterogeneity within the same rock units  
261 and would require more systematic sampling and analysis to provide a detailed and realistic distribution  
262 of the rock petrophysical properties (Rusillon, 2017; Makhoulfi et al., 2018). We instead define two  
263 reference models that represent a typical average aquifer for the Molasse and Malm units, referred as  
264 Molasse0 and Malm0, respectively (Table 2). We only consider sandstone beds as a potential aquifer  
265 for the Molasse, and therefore marls and silstones are disregarded when evaluating the permeability and  
266 porosity of the Molasse aquifers. The aquifer flow velocity and salinity have been set to zero for the  
267 reference models. Molasse0 has a 25 m thick aquifer, whose top is set at 250 m depth. The aquifer  
268 permeability and porosity are 200 mD and 0.20, respectively (Table 2). The aquifer of Malm0 is 100 m  
269 thick, with its top at 1100 m depth, has a permeability of 10 mD and a porosity of 0.15 (Table 2).

Simulation	$h_{top}$	$h_{aq}$	$d_{aq}$	$k$	$\phi$	$v_{aq}$	$c$	$Q_{inj}$	$T_{warm}^*$	$T_{cold}$	$bhp_{min}^*$	$bhp_{max}^*$	$T_{lim}^*$
	m	m	m	mD	-	$m a^{-1}$	-	$L s^{-1}$	$^{\circ}C$	$^{\circ}C$	bar	bar	$^{\circ}C$
Molasse0	50	25	250	200	0.2	0	0	15	90	14.35	1	75	none
Malm0	50	100	1100	10	0.15	0	0	10	90	39.26	1	250	none

**Table 2:** Physical parameters for Molasse0 and Malm0. \*: fixed parameters in all simulations of the parametric study.

270 The investigated values in the parametric study for the aquifer thickness, depth, permeability and porosity  
271 (Tables 1-2) represent the lower and upper bounds of averaged Malm carbonate or Molasse sandstone  
272 aquifers (Brentini, 2018; Rusillon, 2017). The investigated values for the aquifer flow velocity are close  
273 to and above the critical velocity value for heat storage ( $18 m a^{-1}$ ), estimated by Courtois et al. (2006).  
274 No data for the flow direction and velocity are available for the Malm aquifers, whereas the discharge  
275 rate measurements (from drilled wells) in the Molasse units are too scarce to conclude on a realistic value  
276 of the aquifer flow velocity. Water salinity range from 0.3 to  $40 g L^{-1}$  in the Malm units (Rusillon,  
277 2017). Only one sample was measured for the Molasse deposits and gave a salinity lower than  $1 g L^{-1}$   
278 (GeoMolTeam, 2015). These values are typical for sedimentary basins and generally too low to strongly  
279 affect the water density or viscosity (Spivey et al., 2004). Major thrusts in the basement cross-cut the  
280 entire sedimentary cover and have been suggested to be a path for migration of deep and warm fluids  
281 from the basement to shallower units (Chelle-Michou et al., 2017). These thrusts could potentially  
282 drive high-salinity fluids from the Keuper evaporites, resulting in local high-salinity regions where the  
283 concentration is higher than the measured values. Therefore, we present here simulations with salinity  
284 higher than the maximum measured values that could potentially affect the HT-ATES performance.  
285 Additional simulations with salinity in the range of those measured in the GGB (not reported here) show  
286 no significant effects on the HT-ATES performance compared to freshwater simulations.

287 The low permeable rock and padding layers (1,2,4,6, Fig. 3a) have an extremely low porosity (0.01)  
288 and permeability (0.001 mD) in all simulations to ensure that negligible flow occurs in these parts of  
289 the model. The drinking water aquifer (5, Fig. 3a), when considered, has the same permeability and  
290 porosity as the storage aquifer. The upper low-permeability layer (3, Fig. 3a) has a thickness of 50 m  
291 for the reference models and vary between 0 and 50 m in other configurations. The thermal properties  
292 of rocks in the GGB are poorly constrained. We thus use a typical average heat capacity and thermal  
293 conductivity (Table 1) for sedimentary rocks (Kappelmeyer and Haenel, 1974). The water heat capacity  
294 and thermal conductivity show negligible changes for the investigated temperature, pressure and salinity  
295 ranges (Driesner, 2007). Thermal parameters are kept constant in all simulations (Table 1). We impose  
296 an upper bhp limit at 75 and 250 bars for the investigated Molasse and the Malm aquifers, respectively,  
297 during the loading and unloading phases. These limits correspond in average to the estimated lithostatic  
298 pressures at the top of the aquifer. The injection and production rates are scaled with the aquifer depth

299 and permeability, so that the bhp limit is not reached too rapidly in the simulations. The rates are set  
300 to 5, 15 and 20 L s<sup>-1</sup> for permeabilities of 10, 200 and 500 mD, respectively, for the Molasse aquifers.  
301 They are set to 5, 10 and 15 L s<sup>-1</sup> for permeabilities of 2, 10 and 50 mD respectively, for the Malm  
302 aquifers.

## 303 4 Results of the parametric study

304 Fourteen simulations, including the reference model, were performed for each aquifer type. We succes-  
305 sively investigate the effects of the aquifer geometry (depth and thickness) and properties (permeability,  
306 porosity, flow velocity and salinity), as well as the thickness of the upper low-permeability layer. In each  
307 simulation, only one of these parameters varies to evaluate its effect on the HT-ATES performance and  
308 environmental impact.

### 309 4.1 Reference models

310 When injecting warm water into a colder aquifer, a thermal perturbation forms at the well and progres-  
311 sively radially expands inside the aquifer. The maximal distance reached by this perturbation front (or  
312 thermal radius) mostly depends on the aquifer thickness, the volume of injected water and the temper-  
313 ature contrast between this water and the aquifer (Fig. 4). To compare the thermally affected area in  
314 the different simulations, we define as the heat plume the region of the aquifer where the temperature  
315 is at least 30% higher than the average aquifer temperature. This 30% increase ensures that we only  
316 capture the thermal perturbation due to heat storage and not the temperature variations at the top or  
317 bottom of the aquifer, that can show up to 25% deviation from the averaged temperatures depending on  
318 the model configuration and prescribed thermal gradient. The radius of this heat plume is referred to  
319  $R_{th,30}$  to distinguish from the true thermal radius  $R_{th}$ .

320 A larger volume of warm water is injected into a thinner aquifer for Molasse0 than for Malm0, which  
321 results in a wider heat plume. At the beginning of the unloading phase of the 10<sup>th</sup> cycle,  $R_{th,30}$  is equal  
322 to 102 m for Molasse0 and to 34 m for Malm0 (Fig. 4). For both models,  $R_{th,30}$  is only reduced by  
323 approximately 10% at the end of the unloading phase. The contact surface between the aquifer and the  
324 low-permeability rocks is larger for Molasse0 than for Malm0, which leads to a higher thermal perturbation  
325 into the low-permeability rock units (Fig. 4). As only a part of the injected heat is recovered at each  
326 cycle, the heat plume is expected to grow further away from the well and the aquifer will overall warm  
327 up with time. The temperature at the warm well generally increases with time but strongly fluctuates  
328 during the loading and unloading phases (Fig. 5a). Smooth temperature variations also occur during  
329 the resting phases. The temperature variations in the warm well show larger amplitudes for Molasse0  
330 than for Malm0 because the temperature contrast between the injected water and the aquifer is larger.

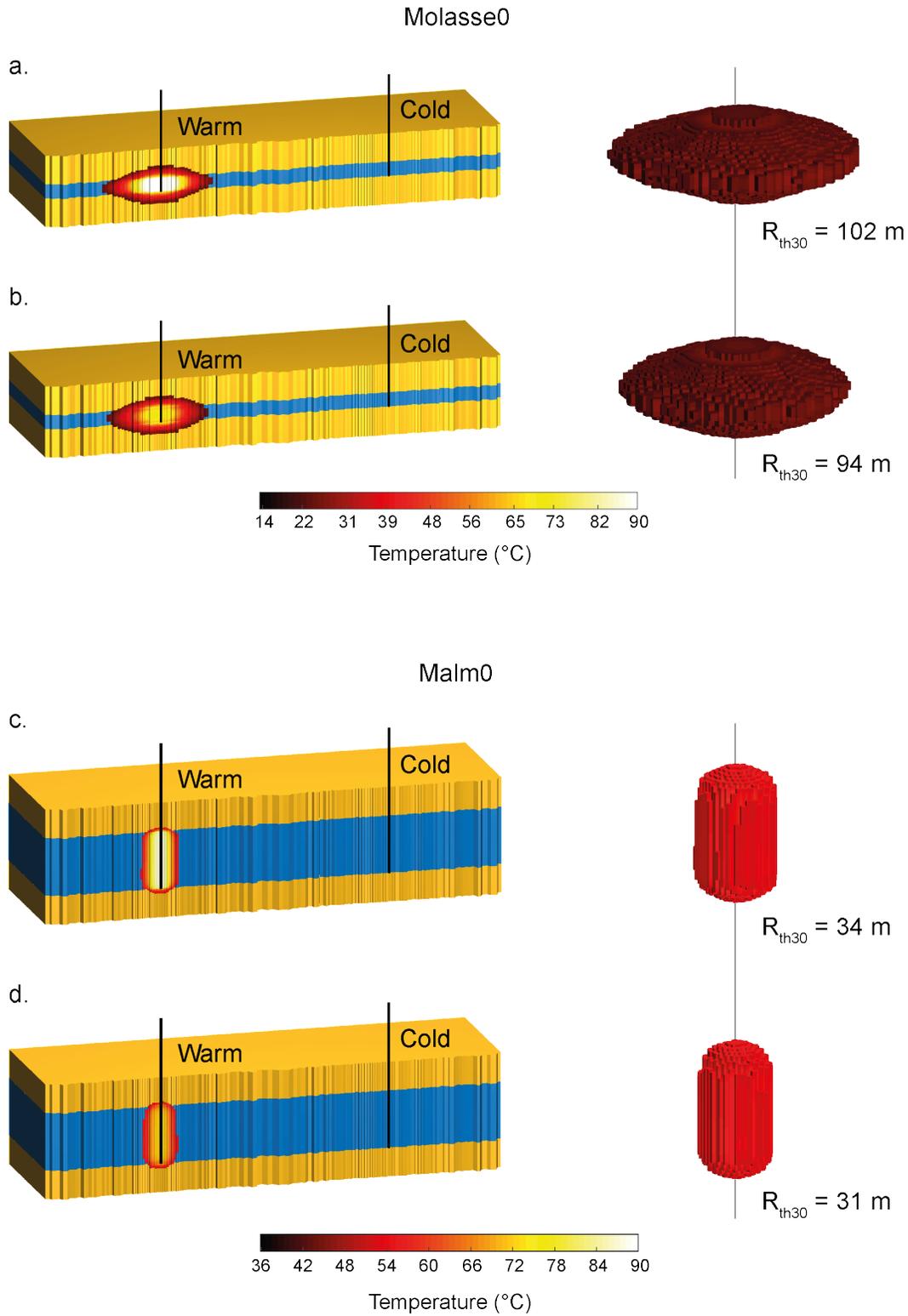


Figure 4: Left: Vertical cross-sections of Molasse0 and Malm0 at the beginning (a,c) and end (b,d) of the unloading phase for the 10<sup>th</sup> cycle. Right: Extracted corresponding heat plume defined as a 30% increase of the initial average temperature in the aquifer ( $R_{th30}$ ).

331 For Molasse0, the temperature at the warm well fluctuates between 48 and 90°C at the beginning of  
332 the HT-ATES exploitation and between 70 and 90°C towards the end. For Malm0, it varies between 60  
333 and 90°C during the first year, but does not drop below 77°C during the last five years of simulation  
334 (Fig. 5a). The temperature at the cold well overall decreases with time because the injected water is  
335 slightly colder than the aquifer average temperature. Temperature variations in the cold well are very  
336 small for both aquifers (max. 2.65 °C) and negligible compared to those at the warm well (min. 12°C)  
337 (Fig. 5b,c).

## 338 4.2 Energy stock

339 Fig. 6 reports the range of values for  $R_{th,30}$  during the entire HT-ATES exploitation for all simulations.  
340  $R_{th,30}$  shows greater variations for the Molasse than for the Malm aquifers because they are generally  
341 thinner and the volume of injected water larger. The main parameters controlling  $R_{th,30}$  are the thickness,  
342 depth, permeability and flow velocity of the aquifer. The absence of an upper low-permeability layer plays  
343 a role in the case of a 25 m thick aquifer with a large volume of injected water (Fig. 6a). However, it  
344 has almost no effect for a 100 m thick aquifer with a small to moderate volume of injected water (Fig.  
345 6b). The aquifer porosity and salinity have little to no effects on  $R_{th,30}$ . For the Molasse aquifers,  $R_{th,30}$   
346 varies between  $\sim 50$  and  $\sim 120$  m during the HT-ATES exploitation for Molasse0 but decreases to  $\sim 20$   
347 m for a low permeability aquifer (10 mD) and increases up to  $\sim 200$  m for a very thin (10 m) aquifer  
348 (Fig. 6a). Variations of  $R_{th,30}$  during the HT-ATES exploitation are also the smallest and the largest for  
349 the low permeability and thin aquifers, respectively. For the Malm aquifers,  $R_{th,30}$  ranges from  $\sim 10$  to  
350  $\sim 40$  m during the HT-ATES exploitation for Malm0 (Fig. 6b), but can reach almost 80 m for aquifers  
351 with a high flow velocity ( $> 50 \text{ m a}^{-1}$ ). For deep aquifers ( $d_{aq} = 1500 \text{ m}$ ), the thermal plume may  
352 even disappear after an unloading phase, as the temperature contrast between the injected water and the  
353 aquifer decreases. Smallest and largest variations of  $R_{th,30}$  during the HT-ATES exploitation are observed  
354 for the thickest aquifer and the aquifer with the highest flow velocity, respectively (Fig. 6b).

## 355 4.3 Thermal performance

356 We also evaluate the thermal performance of the HT-ATES in terms of storage capacity and thermal  
357 recovery. The storage capacity is defined as the maximum stored energy per cycle, which is primarily  
358 controlled by the injection rate. This latter is a function of the aquifer permeability and depth, and the  
359 imposed bhp limit. For the Molasse aquifers, the storage capacity per cycle is  $\sim 50$  TJ on average. It  
360 reaches almost 75 TJ for an aquifer with a 500 mD permeability but drops below 10 TJ when the aquifer  
361 permeability is around 10 mD (Fig. 7a). For the Malm aquifers, the storage capacity is less than half of  
362 that observed for the Molasse aquifers, with nearly 20 TJ on average. It drops to  $\sim 10$  TJ for an aquifer

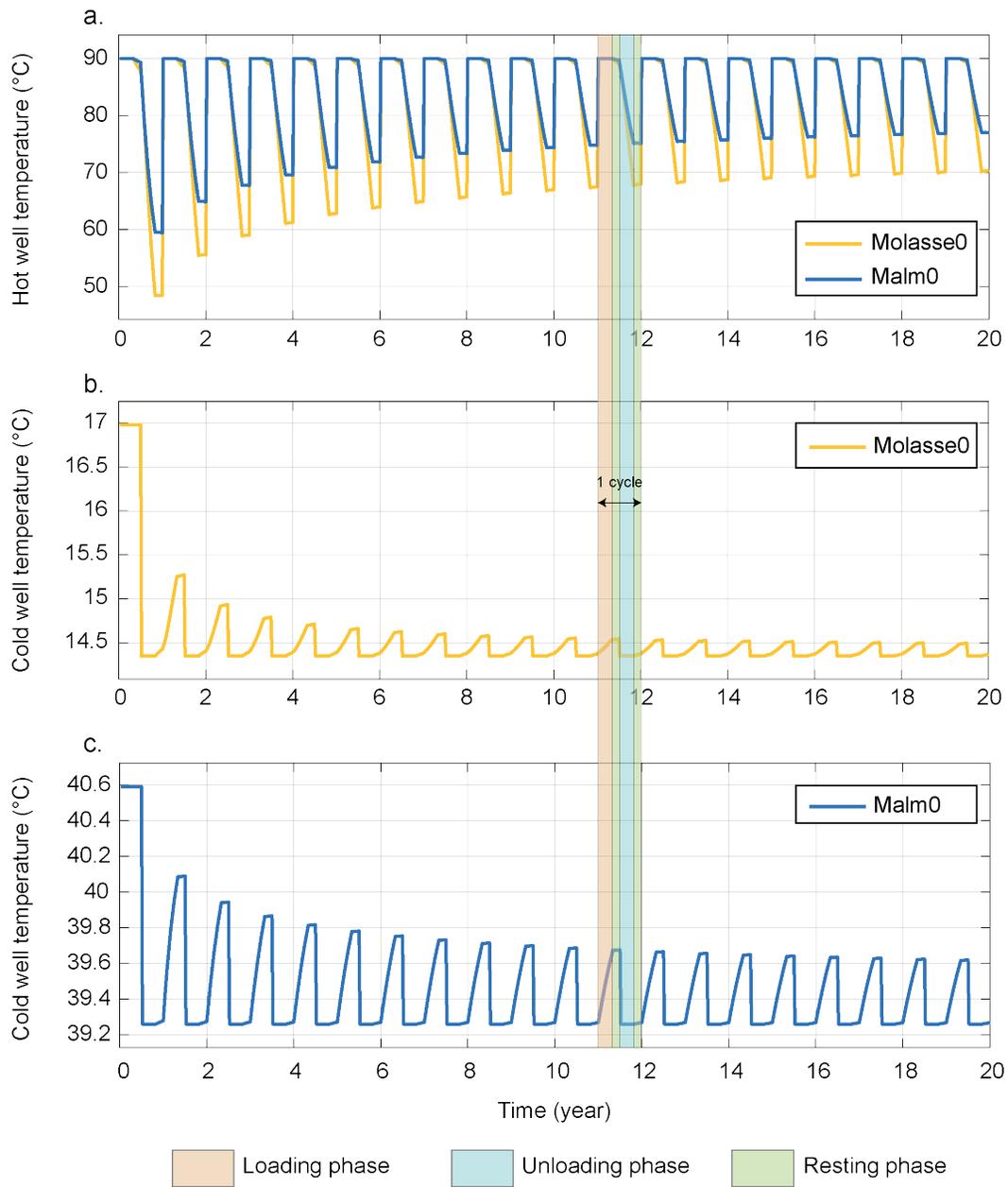


Figure 5: Temporal evolution of the temperature at the warm (a.) and cold (b,c.) wells for both reference models.

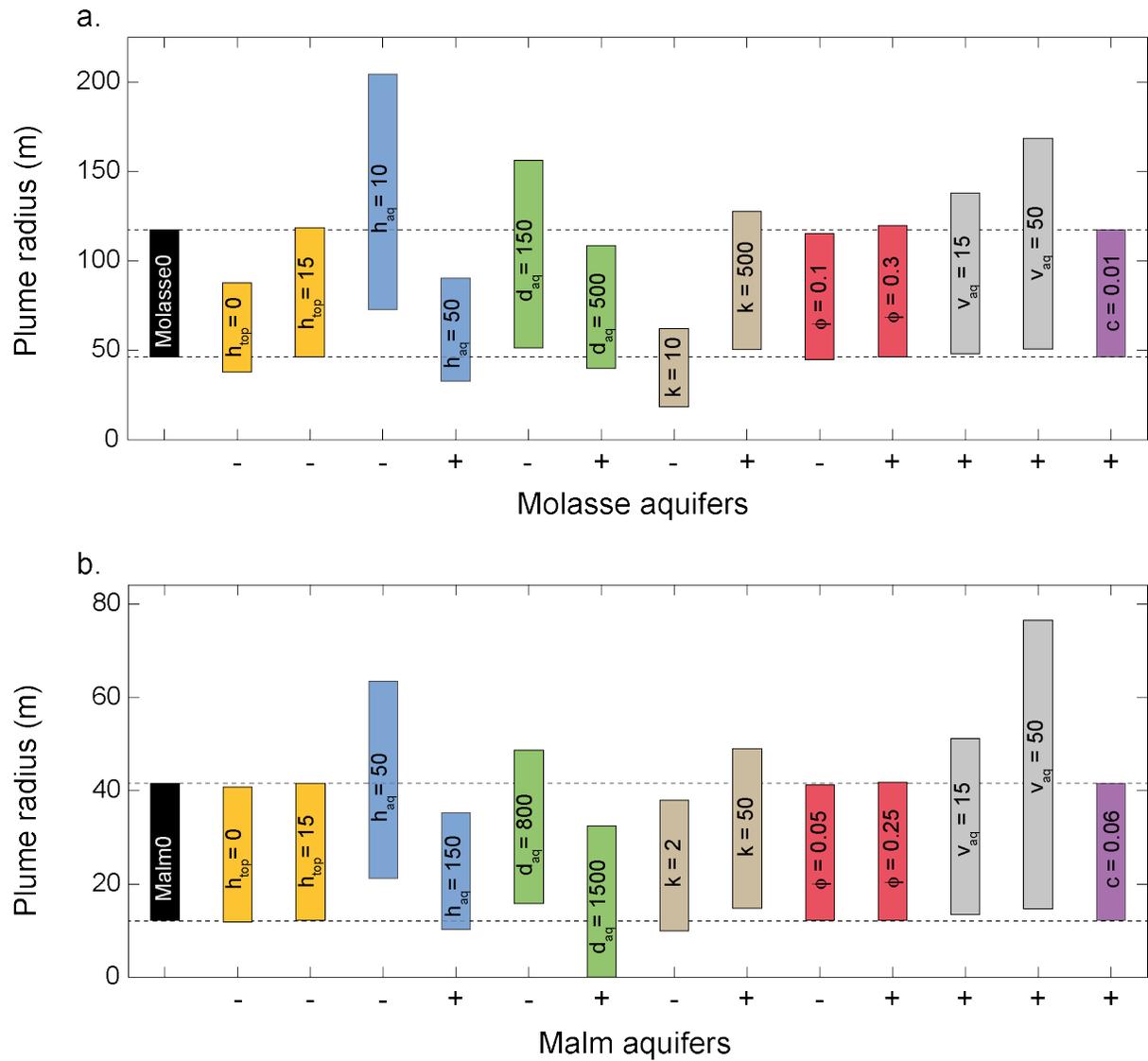


Figure 6: Variations of the heat plume radius ( $R_{th30}$ ) during the HT-ATES exploitation for the different Molasse (a.) and Malm (b.) aquifers. The bars represent the range of values of the plume radius during the HT-ATES simulation. Each colour corresponds to an investigated parameter. Black: reference model, yellow: thickness of the upper low-permeability layer, blue: aquifer thickness, green: aquifer depth, brown: aquifer permeability, pink: porosity, grey: aquifer flow velocity and purple: aquifer salinity. Investigated parameters are given in the figure for each simulation, with a plus or minus sign to indicate if the simulated value is higher (+) or lower (-) than the corresponding value in the reference model. Units and other constant parameters are given in Tables 1-2.

363 permeability around 2 mD and reaches almost 35 TJ for an aquifer with a 50 mD permeability (Fig.  
 364 7b). Although the imposed injection/production rates and aquifer permeabilities are identical, smaller  
 365 variations in the storage capacity are observed for aquifers with different thicknesses and depths than the  
 366 reference models (Fig. 7a,b). This can be explained by the use of fixed bhp limits. When changing the  
 367 aquifer depth or thickness, the water pressure in the wells may deviate significantly from the well pressure  
 368 in the reference models and may reach the bhp limit at a different time of the simulated loading/unloading  
 369 phase. This results in different volumes of injected water and thus of stored energy.

370 The thermal recovery is evaluated through the non-dimensional energy recovery factor,  $\eta$ , which is defined  
 371 as the ratio of the produced to the injected energy during each cycle:

$$\eta = \frac{E_{\text{prod}}}{E_{\text{inj}}} = \frac{\int_0^{t_{\text{prod}}} P_{\text{prod}}(t) dt}{\int_0^{t_{\text{inj}}} P_{\text{inj}}(t) dt}, \quad (7)$$

372 with  $P_{\text{inj}}$  and  $P_{\text{prod}}$ , the thermal power at the loading or unloading phase, respectively, of each cycle,  
 373 which is defined as:

$$P_{\text{prod}}(t) = \rho_f C_f Q_{\text{prod}}(t) |T_{\text{prod}}(t) - T_{\text{aq}}^0| \quad \text{and} \quad P_{\text{inj}}(t) = \rho_f C_f Q_{\text{inj}}(t) |T_{\text{inj}}(t) - T_{\text{aq}}^0| \quad (8)$$

374 with  $Q_{\text{prod}}$  and  $Q_{\text{inj}}$  the production and injection rates measured at the warm well and  $T_{\text{aq}}^0$  the aquifer  
 375 temperature at the beginning of the loading/unloading phases.

376 No cut-off temperature is imposed during the unloading phases. This ensures that the produced volume  
 377 of warm water is similar to the one injected during the loading phase, effectively limiting the overall  
 378 temperature increase in the aquifer. However, a cut-off temperature is used in the post-processing when  
 379 calculating  $\eta$ . Here, we aim at evaluating the thermal recovery for a specific application, namely, directly  
 380 re-injecting the warm water into the pipe network of one of the district heating systems near Geneva to  
 381 provide heat to buildings. Currently, the supply temperature of the CADSIG and CADIOM networks is  
 382 around 100-110°C in winter but could drop to 70-80°C with an optimisation of the network temperatures  
 383 (Faessler et al., 2015). This latter temperature range corresponds to the supply temperature of the  
 384 Cartigny and Aire-la-ville networks in winter and is also more typical for third generation district heating  
 385 (3GDH) systems (Lund et al., 2018). We thus evaluate the thermal recovery with a cut-off temperature  
 386 at 80°C. The excess of produced energy (for  $T < 80^\circ\text{C}$ ) is here considered wasted.

387 The energy recovery factor improves with time as the temperature contrast between the injected water  
 388 and the aquifer decreases. For most of the investigated aquifers,  $\eta$  rapidly increases in the first years and  
 389 reaches its maximum before 15 years (Fig. 8). The energy recovery factor is usually smaller than 0.2 for  
 390 the first year (with the exception of two Malm aquifers) and does not exceed 0.4 after five years (Fig. 8).  
 391 After 20 years,  $\eta$  varies between 0.24 and 0.54 for the Molasse aquifers and between 0.23 and 0.79 for the  
 392 Malm aquifers (Fig. 8). The lowest energy recovery factor is observed for the Malm aquifer with a flow  
 393 velocity of 50 m a<sup>-1</sup>, where  $\eta = 0.23$  after 20 years.

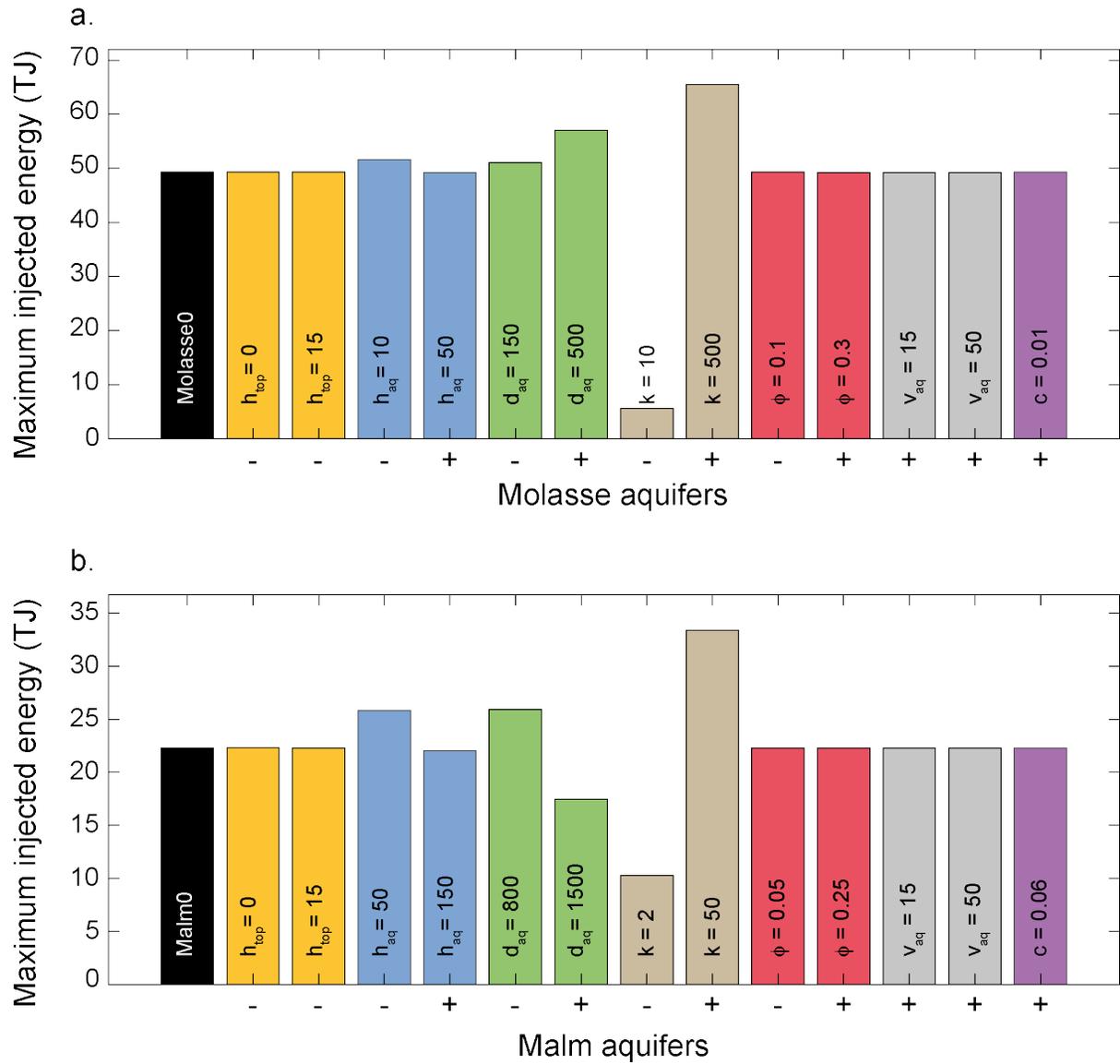


Figure 7: Maximum injected energy during a loading phase for the different Molasse (a.) and Malm (b.) aquifers. Investigated parameters are given in the figure for each simulation. Units and other constant parameters are given in Tables 1-2. Legend for the bar colours is given in Fig. 6.

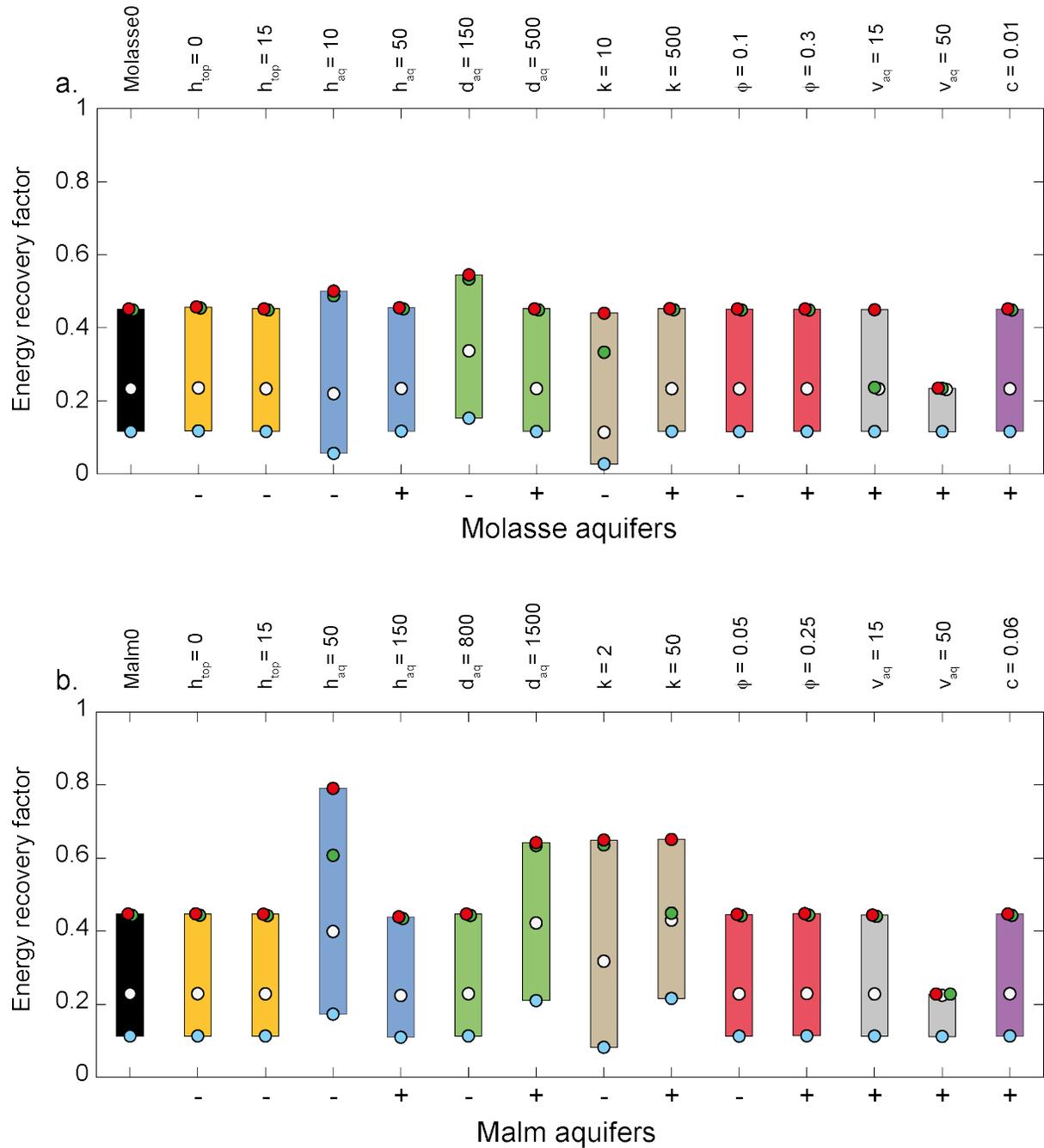


Figure 8: Energy recovery factor for the different Molasse (a.) and Malm (b.) aquifers after 1 (blue dots), 5 (white dots), 15 (green dots) and 20 (red dots) years, evaluated with a cut-off temperature at  $T_{lim} = 80^{\circ}\text{C}$ . Investigated parameters are given in the figure for each simulation. Units and other constant parameters are given in Tables 1-2. Legend for the bar colours is given in Fig. 6.

394 For the Molasse aquifers, the shallowest aquifer ( $d_{\text{aq}} = 150$  m) shows the best thermal performance after 20  
395 years, with  $\eta$  reaching 0.54 (Fig. 8a). This observation may seem counter-intuitive because at shallower  
396 depths the temperature contrast between the injected water and the aquifer is higher and thus the heat  
397 loss by conduction is expected to be larger than for Molasse0, resulting in a lower recovery. However,  
398 the quantity of injected/produced energy are also controlled by the bhp. In the case of a shallower  
399 aquifer, the pressure will be lower than for Molasse0 and the bhp limit might be reached later, resulting  
400 in a larger extracted volume of water. The thinnest Molasse aquifer ( $h_{\text{aq}} = 10$  m) has a slightly better  
401 energy recovery factor after twenty years than Molasse0, although it is lower for the first year (Fig. 8a).  
402 The surface contact between the aquifer top/bottom and the low-permeability rocks is larger than for  
403 Molasse0, resulting in a higher heat loss by conduction and thus a smaller recovery factor at the beginning  
404 of the HT-ATES exploitation. However, with time this heat loss is minimised as the low-permeability  
405 rock heats up, which increases the recovery factor.

406 For the Malm aquifers, the thinnest aquifer ( $h_{\text{aq}} = 50$  m) records the highest recovery factor after 20 years  
407 ( $\eta = 0.79$ ) and also a better recovery factor than Malm0 after the first year (Fig. 8b). This behaviour  
408 can be explained by a better geometry of the energy stock. The heat plume is not as narrow as for  
409 Malm0 and temperature variations inside the aquifer are lower, which results in less heat conduction.  
410 The deepest aquifer ( $d_{\text{aq}} = 1500$  m) has a better energy recovery factor after 20 years than most other  
411 Malm aquifers, which can be explained by the lowest temperature contrast between the aquifer and  
412 injected water, leading to a smaller heat loss by conduction in the aquifer (Fig. 8b). Both Malm aquifers  
413 with a low and high permeability have a better energy recovery factor after twenty cycles than Malm0.  
414 This can be explained by the difference in injected volumes and injection rates controlled by the bhp  
415 limits (Fig. 8b).

416 Neither the thickness of the top layer, the aquifer porosity nor the salinity influence the energy recovery  
417 factor in our simulations. With the exception of the aquifer with no top layer, this lack of variation is  
418 expected, as no changes were observed in the size of the heat plume or the maximal injected energy for  
419 these simulations. For the case without an upper low-permeability layer, the more spherical shape of the  
420 stock may result in a better energy recovery factor and may compensate for the heat loss by convection  
421 and conduction in the upper part of the aquifer.

#### 422 **4.4 Impact on the environment**

423 We monitor the temperature at two points in the model (see Fig. 3a) to evaluate the environmental  
424 impact of the HT-ATES exploitation. The first monitoring point (M1) is centred in the aquifer, 100 m  
425 away from the warm well in the direction of the cold well. We measure here the temperature increase  
426 at the end of the HT-ATES exploitation relative to the initial temperature. This allows us to control  
427 if the HT-ATES complies with the Swiss regulations, which specify that geothermal activities should

428 not modify the natural groundwater temperature of more than 3°C (CH-GSchV, 1998; OFEV, 2009).  
 429 Temperature variations can, however, be higher locally, within a distance of 100 m from the wells. No  
 430 monitoring point is placed close to the cold well as we observe in the reference models that the maximum  
 431 temperature variation at this well was lower than 3°C (Fig. 5). The second monitoring point (M2) is  
 432 placed 30 m above the warm well, and is used to estimate the efficiency of the insulating rock layer  
 433 between two overlying aquifers. The temperature increase at this point is recorded throughout the HT-  
 434 ATES exploitation. Finally, we also monitor the increase in the average aquifer temperature throughout  
 435 the simulations. For M2 and the average aquifer temperature, we only report the maximum temperature  
 436 increase (Fig. 9).

437 Temperature variations are much higher in the Molasse than in the Malm aquifers as the volume of  
 438 injected warm water is larger and the initial aquifer temperature lower (Fig. 9). Only a few of the Molasse  
 439 aquifers comply with the Swiss regulation: the aquifer without an upper low-permeability layer, the low  
 440 permeability aquifer and the aquifer with the highest flow velocity (Fig. 9a). The temperature increase  
 441 above the warm well does not exceed 10°C in the Molasse aquifers, with the exception of the aquifer  
 442 without an insulating top layer where it reaches almost 60°C. The average temperature of the aquifer  
 443 generally does not increase more than 10°C with the exception of the thinnest aquifer ( $h_{\text{aq}} = 10\text{m}$ ) and  
 444 the shallowest ( $d_{\text{aq}} = 150\text{m}$ ) (Fig. 9a). The investigated Malm aquifers comply with the Swiss regulations  
 445 (Fig. 9b). The maximum temperature increase above the warm well does not exceed 4°C in the Malm  
 446 aquifers, with the exception of the aquifer without an upper low-permeability layer, which records a  
 447 temperature increase of approximately 10°C. The Malm aquifers record a maximum increase between 2  
 448 and 4°C of their average temperature (Fig. 9b).

## 449 5 Discussion

### 450 5.1 General observations and comparison with previous studies

451 The environmental impact of the HT-ATES is positively correlated with the plume radius,  $R_{\text{th},30}$ . There-  
 452 fore, storing a large volume of heat into a thin, shallow and permeable aquifer might have a strong impact  
 453 on the environment, and will not comply with the legal regulations in Switzerland.

454 The energy recovery factor depends on the shape of the thermal volume because energy losses by mechan-  
 455 ical dispersion and conduction mostly occur at the boundary of the injected volume of water (Doughty  
 456 et al., 1982; Bloemendal and Hartog, 2018). Assuming the injected volume can be simplified by a cylinder,  
 457 Doughty et al. (1982) showed that the thermal recovery is inversely proportional to the ratio of thermal  
 458 area to thermal volume:

$$\frac{A_{\text{th}}}{V_{\text{th}}} = \frac{2\pi R_{\text{th}}^2 + 2\pi R_{\text{th}} h_{\text{aq}}}{\pi R_{\text{th}}^2 h_{\text{aq}}}, \quad (9)$$

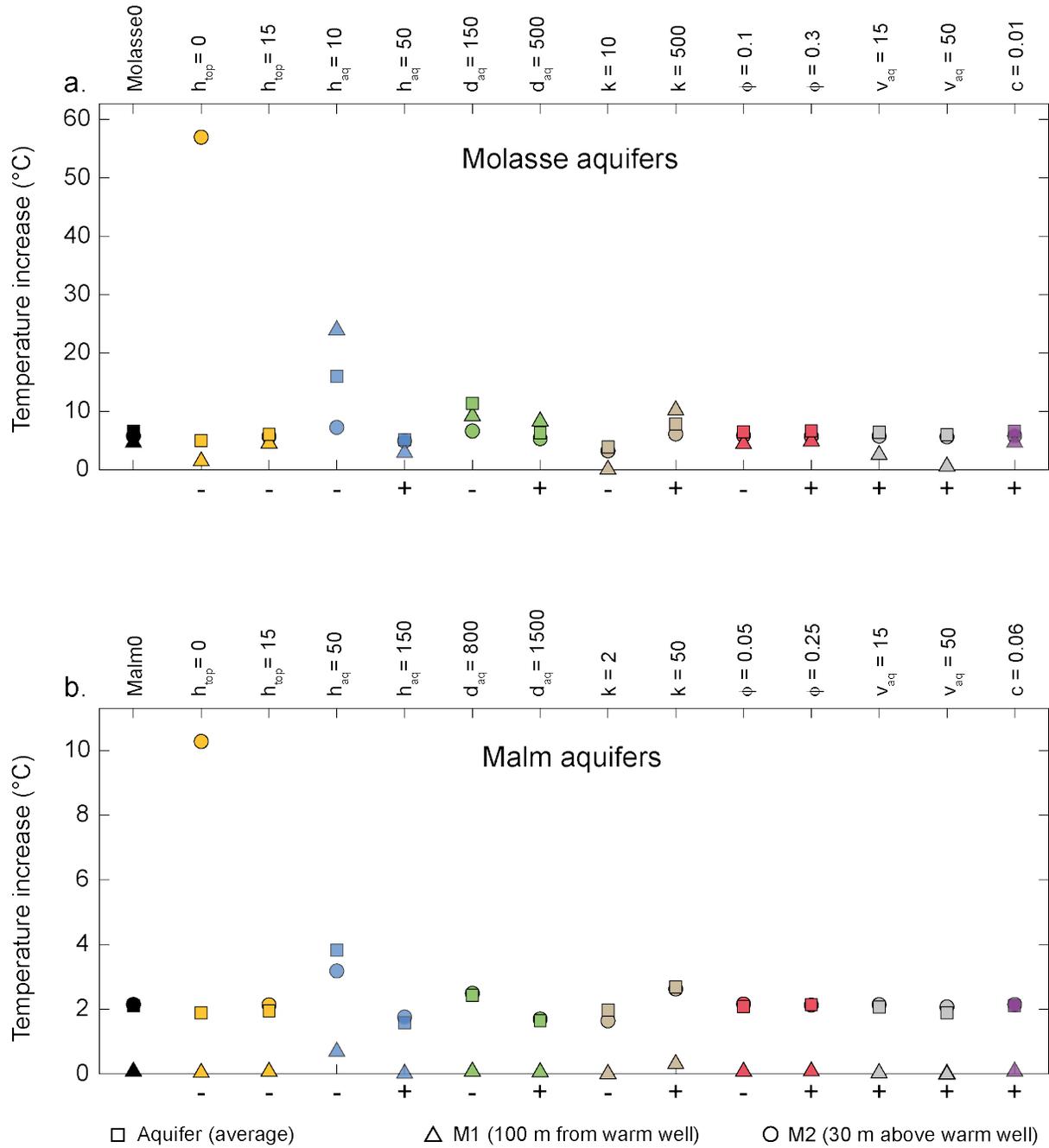


Figure 9: Monitoring of the temperature increase at different locations and times of the ATEs exploitation for the Molasse (a.) and Malm (b.) aquifers. Circles: maximum temperature increase recorded 30 m above the warm well during the ATEs exploitation. Triangles: temperature increase recorded 100 m away from the warm well at the end of the ATEs exploitation. Squares: maximum increase of the aquifer average temperature during the ATEs exploitation. Investigated parameters are given in the figure for each simulation. Units and other constant parameters are given in Tables 1-2. Legend for the point colours is given in Fig. 6.

459 where  $h_{\text{aq}}$  is the aquifer thickness and  $R_{\text{th}}$  the thermal radius defined in eq. (6). The relationship is  
 460 valid for equal injected and produced volumes and assuming that the injection well is perforated over  
 461 the entire aquifer thickness. Buoyancy forces are also neglected. Doughty et al. (1982) also consider  
 462 constant and equal injection and production rates, as well as a constant injection temperature. As such,  
 463 these results are not directly applicable to our study. First, the energy recovery factor is evaluated with  
 464 a cut-off temperature at 80°C so that the produced volume is much smaller than the injected volume.  
 465 Secondly, even if equal injection and production rates are initially prescribed, they may vary during the  
 466 cycles as bhp limits also restrict the pressure range in wells. Therefore, the injected/produced volumes  
 467 in our simulations are usually smaller than the ones predicted by the relation  $V = Qt$  as the bhp limits  
 468 are often reached before the end of the injection period. This shows the importance of appropriately  
 469 selecting the injection/production rates for a given reservoir to ensure that a critical pressure is not  
 470 reached. Many of the previous studies consider constant and equal injection/production rates at each  
 471 cycle, and do not mention the use of a limited pressure range (Kim et al., 2010; Sommer et al., 2013,  
 472 among others). However, it is critical to ensure that no rock failure occurs, since this may result in loss  
 473 of the entire thermal stock. The energy recovery factor in our parametric study remains limited because  
 474 of the cut-off temperature, but reaches 0.8 to 0.9 when injected and produced volumes are equal (see  
 475 Figs 10-11), which is similar to previous studies for comparable injected volumes (Doughty et al., 1982;  
 476 Van Lopik et al., 2016; Bloemendal and Hartog, 2018). The lowest energy recovery factor at the first  
 477 cycle is observed for the simulation with the lowest injected volume for both the Malm and Molasse  
 478 aquifers. This is consistent with the results from Doughty et al. (1982) who observed that the thermal  
 479 recovery efficiency increases with the injected volume. Finally, the lowest energy recovery factor after  
 480 twenty cycles is observed for the simulations with a groundwater flow of 50 m a<sup>-1</sup>, which also agrees with  
 481 previous studies (Courtois et al., 2006; Bloemendal and Hartog, 2018).

482 In addition to mechanical dispersion and conduction, thermal losses can also occur by buoyancy flow due  
 483 to a density difference between the warm and cold water. This triggers a tilt of the thermal front, whose  
 484 rate depends on the injected and aquifer water properties and aquifer permeability. This rate is given by  
 485 an analytical characteristic tilting time (Hellström et al., 1979), defined as:

$$t_0 = \frac{h_{\text{aq}}}{\sqrt{k^h k^v}} \frac{C_a}{C_f} \frac{\pi^2 (\mu_0 + \mu_1)}{32G (\rho_0 - \rho_1) g}, \quad (10)$$

486 where  $h_{\text{aq}}$  is the aquifer thickness (m),  $k^h$  and  $k^v$  are the horizontal and vertical aquifer permeabilities  
 487 (m<sup>2</sup>),  $C_a$  and  $C_f$  are the aquifer and fluid volumetric heat capacities (J m<sup>-3</sup> K<sup>-1</sup>), respectively.  $G$  is  
 488 Catalan's constant ( $\sim 0.915$ ),  $g$  is the gravitational constant (9.81 m s<sup>-2</sup>), whereas  $\mu_0/\rho_0$  and  $\mu_1/\rho_1$  are the  
 489 viscosities (kg m<sup>-1</sup> s<sup>-1</sup>)/densities (kg m<sup>-3</sup>) of the ambient and injected water, respectively. The tilting  
 490 angle of an initially vertical front during a time  $t_0$  is  $\sim 60^\circ$  (Hellström et al., 1979). In our simulations, we  
 491 do not observe a tilt of the thermal front during the injection, storage or production phases of the different  
 492 cycles, although we consider a temperature-dependent density and viscosity. This can be explained by

493 the very high characteristic tilting times estimated for the Molasse and Malm aquifers with respect to  
494 the injection period (120 days). Considering the temperature at the top of the aquifer (coldest) as the  
495 ambient temperature in Eq.(10), we estimated  $t_0$  to be at least 5 times higher than the injection time  
496 for the Molasse aquifers, and more than hundred times higher for the Malm aquifers. Such high values  
497 for  $t_0$  can however be explained by the low permeability of the aquifers. The aquifers investigated by  
498 [Hellström et al. \(1979\)](#) that presented strong tilts of the thermal front had permeabilities up to  $10^6$  mD.  
499 Our investigated aquifers, on the contrary, are considered as very low- to low-permeable aquifers (<1000  
500 mD), with a maximum permeability of 500 mD. For comparison, a 40 m thick aquifer with an isotropic  
501 permeability of 100 mD (equivalent to Molasse0) and injection and ambient temperatures at 120 and  
502  $20^\circ\text{C}$ , respectively, yields a tilt angle lower than  $2^\circ$  after 270 days ([Hellström et al., 1979](#)). Our injection  
503 temperature being lower, the tilt is expected to be even smaller and will not be captured by the current  
504 grid resolution. Simulations at a significantly finer spatial resolution show a very small tilt, but no impact  
505 on the energy recovery factor is observed (see. suppl.mat.).

## 506 5.2 Application of the model to the GGB and beyond

507 The main economical application of the stored energy considered in our study is for direct heating of  
508 buildings, by re-injecting the warm water in one of the district heating systems in the Geneva Canton to  
509 compensate the heat deficit in winter. We consider that the stored water has an initial temperature of  
510  $90^\circ\text{C}$  and it is re-injected at a minimum temperature of  $80^\circ\text{C}$  (based on the operative temperatures of the  
511 different heating networks). Currently, the warm water could be directly re-injected into the Cartigny and  
512 Aire-la-ville networks, or into the CADSIG and CADIOM networks, after optimisation ([Faessler et al.,](#)  
513 [2015](#); [Quiquerez et al., 2015](#)). The parametric study reveals that for the considered well schedules (i.e.  
514 volume recovery factor close to one) and rates, the energy recovery factor generally remains low (<0.6)  
515 because of the high cut-off temperature. The Malm aquifers show a slightly better recovery factor (up  
516 to 0.79) than the Molasse aquifers (<0.54) but have approximately 50% lower energy storage capacity.  
517 Storing the 35Gwh (or 126 TJ) of heat in excess would require approximately three and six pairs of wells  
518 for the Molasse and Malm aquifers, respectively. The Malm aquifers are at more than 1000 m depth and  
519 commonly four times deeper than the Molasse aquifers, and will thus have considerably higher drilling  
520 costs ([Leamon, 2006](#)). Therefore, the Molasse aquifers are probably more economically valuable than  
521 Malm aquifers, despite a lower energy recovery factor (Fig. 8). However, most of the Molasse aquifers  
522 do not comply with the Swiss regulations, which limit the temperature increase below  $3^\circ\text{C}$  100 m away  
523 from the warm well at the end of the HT-ATES exploitation. On the contrary, all Malm aquifers satisfy  
524 this requirement.

525 Limiting the temperature rise and/or increasing the energy recovery factor could be achieved by investi-  
526 gating different well schedules and rates. Injecting at a lower rate or temperature will result in a smaller

527 thermal perturbation. The economical application of the energy stored in the aquifer has a primary  
528 control on the HT-ATES thermal recovery because it determines the range of stored and extracted tem-  
529 peratures, as well as whether or not a cut-off temperature is imposed during the unloading phases. Having  
530 a cut-off temperature when simulating the unloading phases is likely to improve the thermal recovery  
531 factor because the aquifer will overall warm up more rapidly as a lower volume of the stored warm water  
532 is extracted. Similarly, the recovery factor can also be improved if the temperature difference between  
533 the stored water and the economical application is higher, i.e. if either the cut-off temperature is lower  
534 or if warmer water is initially injected in the aquifer. For example, the cut-off limit could be lowered  
535 to 55-60°C for direct heating of 4<sup>th</sup> generation district heating (4GDH) systems (Lund et al., 2018). It  
536 could be further lowered for other low-energy applications such as heating of greenhouses, and coupled if  
537 necessary with heat-pumps depending on the temperature (Courtois et al., 2006). Storing the water at a  
538 warmer temperature would also be possible as the temperature in the CADSIG/CADIOM networks and  
539 outside the Cheneviers plant can be regulated (Faessler et al., 2015; Quiquerez, 2017).

540 We perform additional simulations for both aquifer types to evaluate the impacts of different economical  
541 strategies on the HT-ATES thermal performance and environmental impact. These simulations are  
542 compared with Molasse0 and Malm0 (Figs. 10–11) and the corresponding well parameters are reported  
543 in Table 3. The geometry of the aquifer and its thermal and physical properties are the same as for the  
544 reference models. The first simulation (Molasse1 or Malm1) employs different injection and production  
545 rates. No cut-off temperature is prescribed neither in the simulation nor in the post-processing when  
546 evaluating the energy recovery factor  $\eta$  for the reference models and the first simulation. The other  
547 setups are simulated with injection and production rates equal to the reference models, but with different  
548 injection and cut-off temperatures (Table 3). For the Molasse aquifers, we investigate lower injection  
549 rates and temperatures in an attempt to comply with the swiss regulations. Instead, for the Malm we  
550 investigate higher injection rates and temperatures to improve  $\eta$ .

Simulations	$Q_{inj}$ L s <sup>-1</sup>	$T_{warm}$ °C	$T_{cold}$ °C	$bhp_{min}$ bar	$bhp_{max}$ bar	$T_{lim}$ °C
Molasse0	15	90	14.35	1	75	none
Molasse1	7	90	14.35	1	75	none
Molasse2	15	90	14.35	1	75	80
Molasse3	15	90	14.35	1	75	60
Molasse4	15	70	14.35	1	75	55
Molasse5	15	70	14.35	1	75	30
Molasse6	15	60	14.35	1	75	30
Malm0	10	90	39.26	1	250	none
Malm1	15	90	39.26	1	250	none
Malm2	10	90	39.26	1	250	80
Malm3	10	90	39.26	1	250	60
Malm4	10	120	39.26	1	250	80
Malm5	10	120	39.26	1	250	100

**Table 3:** Parameters employed for the simulations using different schedules. Rock and aquifer properties are the same as for the reference models (Table 2, Fig. 4).

551 The thermal radius  $R_{th,30}$  varies between 30 and 150 m for the Molasse aquifers (Fig. 10a). Only  
552 Molasse2 that employs a cut-off and injection temperatures at 80°C and 90°C, respectively, has a wider  
553 plume radius than Molasse0. Molasse3 and Molasse0 show similar  $R_{th,30}$  variations (Fig. 10a). This can  
554 be explained by the fact that for Molasse0, the temperature in the warm well does not drop below 60°C  
555 after the fourth cycle (Fig. 5). Therefore, a cut-off temperature at 60°C does not affect the volume of  
556 extracted fluid in subsequent cycles. Simulations with a lower injection temperature have slightly lower  
557 plume radius. The energy storage capacity is reduced when decreasing the injection rate or temperature  
558 (22 TJ for Molasse1 against 50 TJ for Molasse0, Fig. 10b). However,  $\eta$  remains almost the same after 15  
559 years (Fig. 10c). All the simulations have a similar  $\eta$  of 0.8 after 15 years, with the exception of Molasse2  
560 that reaches almost 0.9 (Fig. 10c). These are considerably better than for the parametric study (Fig. 8a).  
561 Simulations with a small temperature difference between the injected water and cut-off limit (Molasse2,  
562 Molasse4) tend to have a lower  $\eta$  than Molasse0 during the first years, but they are comparable after 15  
563 years. Only Molasse1 that has an injection rate at 7 L s<sup>-1</sup> complies with the Swiss regulations (Fig. 10d).  
564 Molasse2 records the highest temperature increase for M1 (taken 100 m away from the warm well at the  
565 end of the HT-ATES exploitation) with more than 10°C. The other simulations show a temperature  
566 increase for M1 around 4°C. In addition to the simulations presented here, we also ran a simulation with  
567 the same properties as for Molasse0 but with an injection rate at 10 L s<sup>-1</sup>. The simulation satisfies  
568 the swiss regulations with a temperature increase for M1 of 2.6°C. The maximum injected energy per  
569 cycle reaches 33 TJ, suggesting that four wells will be necessary to store the annual 35 GWh of excess  
570 energy.

571  $R_{th,30}$  ranges from 10 to 50 m for the Malm aquifers (Fig. 11a), and is wider for simulations with a  
572 higher injection rate (Malm1) or when  $T_{lim} \geq 80^\circ\text{C}$  (Malm2, Malm4 and Malm5) than for Malm0. The  
573 largest  $R_{th,30}$  are observed in simulations with injection temperature at  $120^\circ\text{C}$ . The amount of injected  
574 energy increases by approximately 70% (from 22 TJ to 38 TJ) for simulations with a warmer injected  
575 water or a higher injection rate compared to Malm0 (Fig. 11b). Overall,  $\eta$  improves compared to the  
576 parametric study (Fig. 8b) and reaches 0.8 after 15 years (Fig. 11c). A higher injection temperature  
577 yields lower energy recovery factors compared to Malm0 in the first cycles, but they are similar after  
578 five years. Malm2 has a low energy recovery factor after the first year but it improves in the long term  
579 and reaches 0.8. All the Malm aquifers comply with the Swiss regulations (Fig. 11d). The simulations  
580 with the highest injection temperature record the largest temperature increases in the aquifer and above  
581 the warm well (Fig. 11d). This can be explained by both the wider heat plume and higher temperature  
582 difference between the injected water and the aquifer.

583 Generally,  $\eta$  can be improved considerably by either imposing a cut-off temperature during the unloading  
584 phases or by using the extracted water at lower temperature (Figs. 10–11c). Installing 4GDH systems,  
585 operating with supply temperatures around  $55^\circ\text{C}$  (Lund et al., 2018), in new neighbourhoods could  
586 contribute to increase the thermal recovery. It will also allow the storage at lower temperatures, thereby  
587 restricting the thermal perturbation. Other low-temperature applications like greenhouse heating can  
588 also be considered to maximise the use of the produced water. All investigated Malm aquifers comply  
589 with the Swiss regulations and represent an interesting target for storage above  $90^\circ\text{C}$ . Although few of  
590 the Molasse aquifers investigated in the parametric study comply with the Swiss regulations, the Molasse  
591 deposits can still represent a target for heat storage if the volume of injected water is limited. Only  
592 reducing the temperature of the injected water does not effectively limit the temperature increase below  
593 the legal regulations. In this case, the Molasse aquifers are an economically more valuable target for  
594 storage at temperature below  $90^\circ\text{C}$  than the Malm aquifers, which also require at least four wells to store  
595 the annual excess of energy (Fig. 7b).

596 This study represents a first investigation of the storage possibilities in the Molasse and Malm units of  
597 the GGB and highlights the importance of some physical parameters. The porosity when not linked to  
598 permeability, the salinity and the aquifer flow velocity up to  $15\text{ m a}^{-1}$  have no impact on the HT-ATES  
599 performance nor its environmental impact. The values used for the salinity are larger than the measured  
600 values in the GGB (Rusillon, 2017), indicating that this parameter may be neglected in future studies  
601 investigating HT-ATES performance. However, saline water could be a problem from an operational  
602 aspect, as it may cause scaling in wells (Jenne et al., 1992). The energy recovery factor in the long  
603 term is not affected for aquifer flow velocities up to  $15\text{ m a}^{-1}$ , which is consistent with previous studies  
604 (Courtois et al., 2006). However, we notice a time delay to reach the maximum energy recovery factor  
605 for the Molasse aquifers (see Fig. 8a compared to Fig. 8b, and reference models). Finally, a 15 m thick  
606 low-permeability rock unit seems to sufficiently limit the temperature increase in shallower units (same

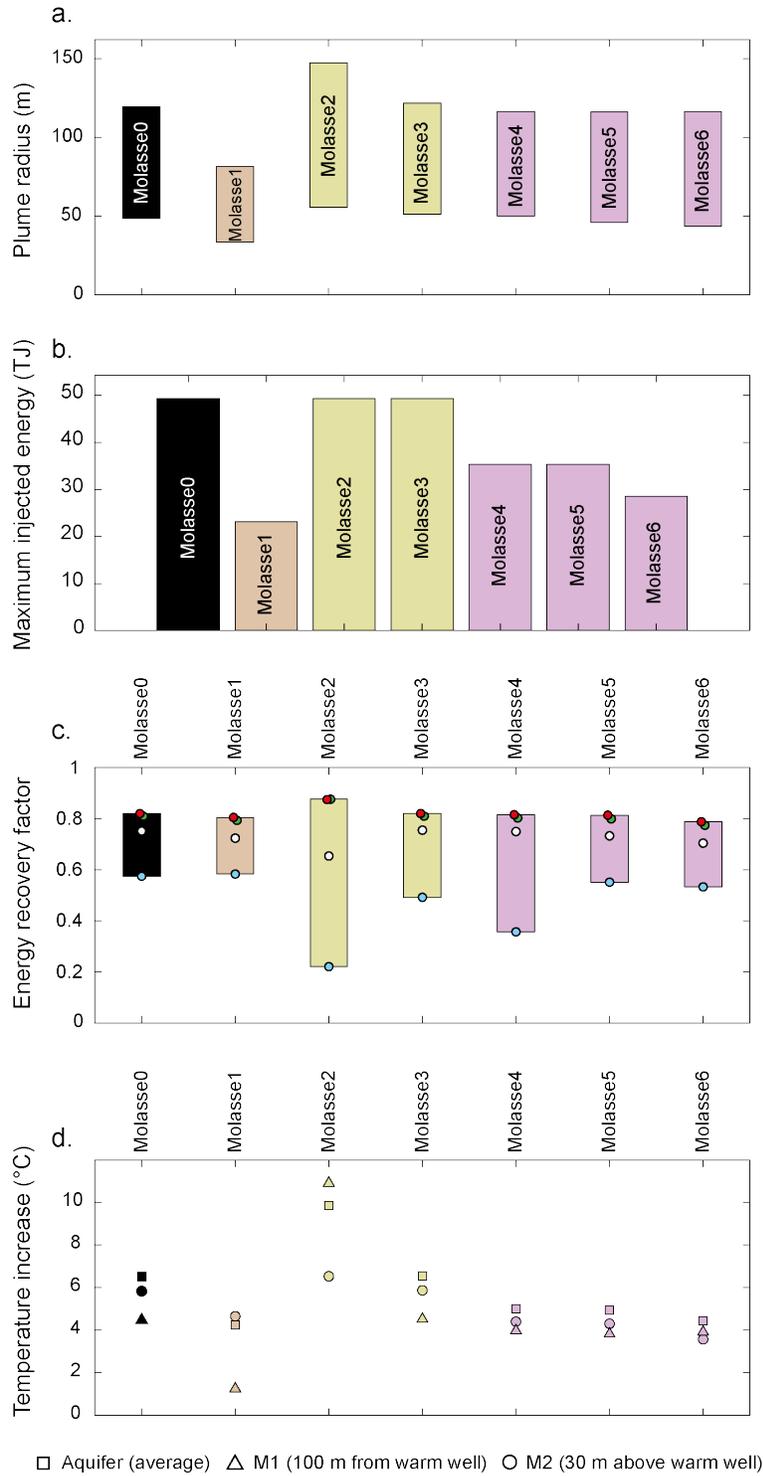


Figure 10: **a.** Variations of the heat plume radius during the ATEs exploitation, **b.** maximal injected energy during a loading phase, **c.** energy recovery factor and **d.** temperature monitoring for a Molasse aquifer with different scheduling strategies. Blue, white, green and red dots: energy recovery factor after 1, 5, 15 and 20 years, respectively. Circles: maximum temperature increase recorded 30 m above the warm well during the ATEs exploitation. Triangles: temperature increase recorded 100 m away from the warm well at the end of the ATEs exploitation. Squares: maximum increase of the aquifer average temperature during the ATEs exploitation. Rock and aquifer properties are the same as for Molasse0. Parameters for the different well schedules are given in Table 3.

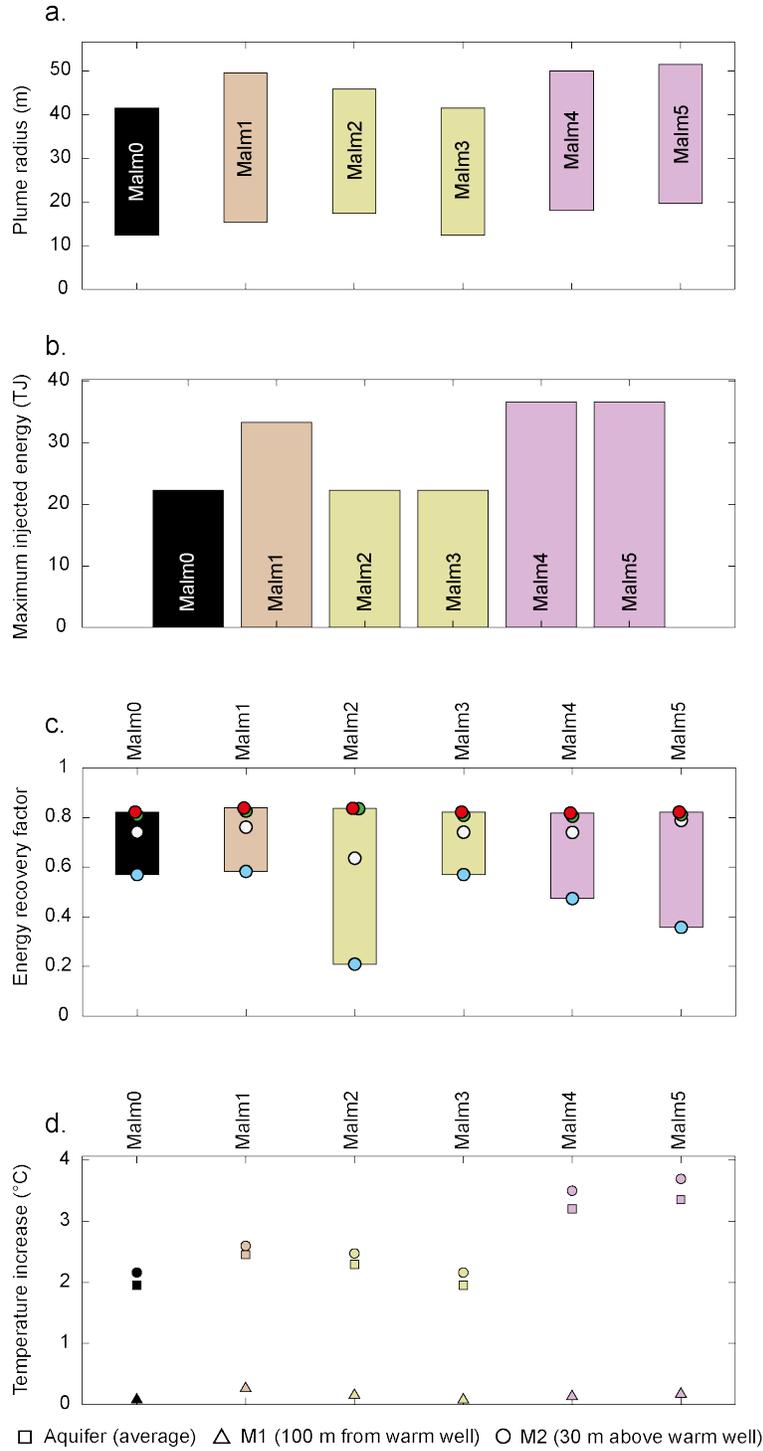


Figure 11: **a.** Variations of the heat plume radius during the ATEs exploitation, **b.** maximal injected energy during a loading phase, **c.** energy recovery factor and **d.** temperature monitoring for a Malm aquifer with different scheduling strategies. Blue, white, green and red dots: energy recovery factor after 1, 5, 15 and 20 years, respectively. Circles: maximum temperature increase recorded 30 m above the warm well during the ATEs exploitation. Triangles: temperature increase recorded 100 m away from the warm well at the end of the ATEs exploitation. Squares: maximum increase of the aquifer average temperature during the ATEs exploitation. Rock and aquifer properties are the same as for Malm0. Parameters for the different well schedules are given in Table 3.

607 environmental impact with a 15 or 50 m thick layer, Fig. 9). The temperature increase 30 m above  
608 the warm well is between 2 and 4°C and between 4 and 6°C for Malm0 and Molasse0, respectively,  
609 depending on the employed well schedule (Figs. 10d–11d). Groundwater chemistry can be altered by  
610 temperatures changes since temperature affects many processes, such as solubility of minerals, reaction  
611 kinetics, oxidation of organic matter, or even redox processes (Brons et al., 1991; Sowers et al., 2006; Bonte  
612 et al., 2013). The magnitude of these effects depends on the initial water chemistry and temperature, as  
613 well as the temperature variations. The effects of temperature on mineral equilibrium remain limited for  
614 small temperature rise and at low temperature (<25°C) (Drijver, 2011; Hartog et al., 2013; Possemiers  
615 et al., 2014). Based on the Arrhenius equation, reaction kinetics are not significantly influenced by  
616 temperature changes lower than 20°C (Possemiers et al., 2014). The use of groundwater for drinking and  
617 process water can be limited for temperature higher than 25°C due to the reduction of metal oxides and  
618 possible release of heavy metals from sediments (Jesušek et al., 2012). The initial temperature of the  
619 shallower aquifer, 30 m above the warm well, is about 14 and 38°C for Molasse0 and Malm0, respectively.  
620 For Molasse0, the maximum temperature increase yields a temperature of 20°C, suggesting that the  
621 temperature will have little influence on the drinking water quality. For Malm0, the initial temperature  
622 is already close to 40°C and likely too high for a good quality of drinking water. In absence of detailed  
623 data concerning the water chemistry in the GGB, it is difficult to predict the impact of a temperature  
624 rise on water quality. Further studies are thus required.

625 The investigated Molasse aquifers are considered to be sandstone channel bars, surrounded by very-low  
626 permeable siltstones and claystones, and thus represent interesting isolated reservoirs for storage. Despite  
627 a small lateral extension, the river beds can be stacked on top of each other, forming a single reservoir.  
628 This allows having a larger, yet laterally localised storage, which can be of great importance for thermal  
629 recovery efficiency or when planning HT-ATES systems in densely populated areas (Doughty et al., 1982;  
630 Sommer et al., 2015). The Molasse deposits constitute a quasi-continuous unit along the Alps Mountains,  
631 from France to Austria, where such alternating sandstone channel bars and clay deposits can be found,  
632 and could be considered for heat storage. In particular, the HeatStore<sup>1</sup> project aims at developing an  
633 ATES experimental site near Bern, Switzerland. Since the Molasse exhibits similar heterogeneities in its  
634 properties across the Alps, the results shown here are relevant for the scientific community working in  
635 other regions. The approach used in this study can be applied to other highly heterogeneous reservoirs of  
636 the Molasse basin. While the legal temperature increase is limited to 3°C in Switzerland for geothermal  
637 application, it can reach up to 11°C in France (Hähnlein et al., 2010), which offers more flexibility. Austria,  
638 on the other hand, is more restrictive and limits geothermal activities in a temperature range between  
639 5 and 20°C. With the necessity to reduce carbon emissions, heat storage is a developing and promising  
640 technology to recycle the large amount of heat wasted by the industrial sector. The prospecting of new  
641 reservoirs is thus important and sand bars of the Molasse deposits could represent a potential target for

---

<sup>1</sup><https://www.heatstore.eu/>

642 low- to moderate-temperature storage ( $<90^{\circ}\text{C}$ ). More generally, this type of reservoir architecture and  
643 sedimentary deposits can be interesting for heat storage due to their high permeability and limited lateral  
644 extension (i.e. isolated reservoir) and are commonly found in foreland basins. Recently, [Winterleitner  
645 et al. \(2018\)](#) investigated the possibility of heat storage in such sandstone channel bars in Oman.

### 646 **5.3 Limitations of the study**

647 The HT-ATES performance and environmental impact for the Molasse and the Malm stratigraphic units  
648 were evaluated using the currently available data for the GGB and considering Swiss regulations. It is  
649 worth noting that the majority of the wells considered by [Rusillon \(2017\)](#), who provided a first review  
650 of the rock permeability and porosity, were drilled in France. Similarly, their outcrop samples mostly  
651 originated from France. Moreover, thermal rock properties for the GGB are not constrained and average  
652 values for sedimentary rocks were taken from the literature for our study. Due to the strong heterogeneity  
653 of the rock properties in the GGB, the extrapolation of the data from [Rusillon \(2017\)](#) and the literature  
654 for our model may not be sufficient to evaluate the full potential and feasibility of heat storage in the  
655 Geneva Canton. More data need to be acquired near Geneva to fully characterise the physical and thermal  
656 properties of the aquifers.

657 Furthermore, some processes are not considered in our model, or have been simplified. The Malm  
658 aquifers are mostly fractured or karstified ([Signer and Gorin, 1995](#); [Signorelli et al., 2004](#)). There is  
659 thus a difference in porosity and permeability between the rock matrix and the fractures, which may  
660 result in different flow velocities. In theory, a dual-porosity model should be employed to investigate the  
661 Malm aquifers for which the fracture size, porosity and permeability are defined. However, in absence  
662 of consistent and reliable data for the fractures, we believe a model of fluid flow in a porous medium is  
663 a fair approximation for a preliminary evaluation of the aquifer potential for heat storage. Constraining  
664 the Malm fractures permeability and porosity is not only important for the choice of the appropriate  
665 model, but is above all crucial to simply evaluate the feasibility of heat storage in these aquifers. High  
666 permeability fractures would result in the loss of the stored heat after the summer. The use of our  
667 model to simulate the Molasse aquifers is however perfectly justified as the investigated reservoirs are  
668 sandstones with little to no fractures ([Platt and Keller, 1992](#); [Chevalier et al., 2010](#)). We have considered  
669 in this study homogeneous isotropic permeabilities and porosities, representative of the average values  
670 for the Malm and Molasse aquifers. In reality, these parameters show strong spatial variations and could  
671 significantly affect the HT-ATES performance and its environmental impact ([Sommer et al., 2013](#)). A few  
672 measurements are available for the permeability anisotropy in the GGB, indicating a ratio of vertical to  
673 horizontal permeability of 0.9 and 1.2 for the Molasse and Malm aquifers, respectively ([Rusillon, 2017](#)).  
674 Simulations (not reported here) with varying horizontal to vertical permeability ratio for both Malm and  
675 Molasse aquifers show no notable effect of this anisotropy on the HT-ATES performance. This is expected,

676 because in a homogeneous aquifer with a well perforated over its entire thickness, the flow is dominantly  
677 lateral during the loading and unloading phases. Although we only considered measurements done on  
678 sandstones to characterise the petrophysical properties of the Molasse aquifers, previous studies revealed  
679 a strong variability, with permeabilities ranging from 0.1 to 1300 mD and porosities between 0.04 and 0.32  
680 (Rusillon, 2017). To evaluate the effect of an heterogeneous aquifer on the performance of a HT-ATES,  
681 we perform two simulations with different permeability and porosity distributions (Fig. 12a,b). All other  
682 aquifer and well parameters are the same as for Molasse0. We generate a field by a Gaussian process,  
683 where 20 independent layers were sampled from the same distribution. Permeability is assumed to be  
684 lognormally distributed, with a normal distribution for the porosity. The porosity is directly correlated  
685 with the logarithm of the permeability and varies between 0.001 and 0.37.

686 Heterogeneous aquifers display a more random distribution of the thermal perturbation due to preferential  
687 flow direction (Fig. 12c,d). The heat plume is no longer cylindrical as in the previous simulations and  
688 its shape is controlled by the most permeable parts of the aquifer. For the first simulation, the aquifer is  
689 quite tight around the injection well and the heat does not propagate very far in the aquifer (Fig. 12c).  
690 Although not completely cylindrical, the shape of the heat plume is similar to those in the previous  
691 homogeneous simulations. The second simulated aquifer has a higher permeability towards the bottom of  
692 the aquifer, whereas its upper part has a very low permeability. This results in a conical thermal plume  
693 (Fig. 12d). The energy stored in the aquifer is  $\sim 25\%$  higher for the second simulation than the first,  
694 mostly due to a higher permeability around the injection well and a generally slightly higher permeability  
695 in the aquifer (Fig. 12a-e). The energy recovery factor  $\eta$  is calculated without any cut-off temperature.  
696 For the first simulation,  $\eta$  still remains below 0.5 after 20 years, which is about 50% of the observed  
697 value for Molasse0 (Fig. 10c, Fig. 12f). For the second simulation,  $\eta$  is only 6% lower than for Molasse0.  
698 This latter difference is in a range of those expected between heterogeneous and homogeneous aquifers  
699 (Sommer et al., 2013). These simulations show the importance of characterising the permeability and  
700 porosity patterns in heterogeneous aquifers so that the wells can be placed ideally to limit the reduced  
701 thermal recovery.

702 Aspects such as rock mechanics or rock-fluid interactions are not addressed in this study. We consider  
703 an upper bhp limit in our model that roughly corresponds to the average lithostatic pressure in the  
704 aquifer, but we do not use a more precise failure criterion. Our model only investigates fluid flow and  
705 is not coupled to a mechanical model that could for example investigate the ground deformation during  
706 loading or unloading phases (e.g. poro-elastic model, (Biot, 1941)). However, as the HT-ATES uses  
707 pairs of wells to ensure a volume balance and limit inflation or deflation in the reservoir, the subsequent  
708 ground deformation should remain limited. Dissolution of rock minerals and subsequent re-precipitation,  
709 as well as microbiological processes may considerably affect the HT-ATES performance by modifying the  
710 permeability and porosity in the aquifer (Brons et al., 1991; Jenne et al., 1992). The intensity and kinetics  
711 of the reactions will depend on the water chemistry, temperature, pressure and pH. These processes

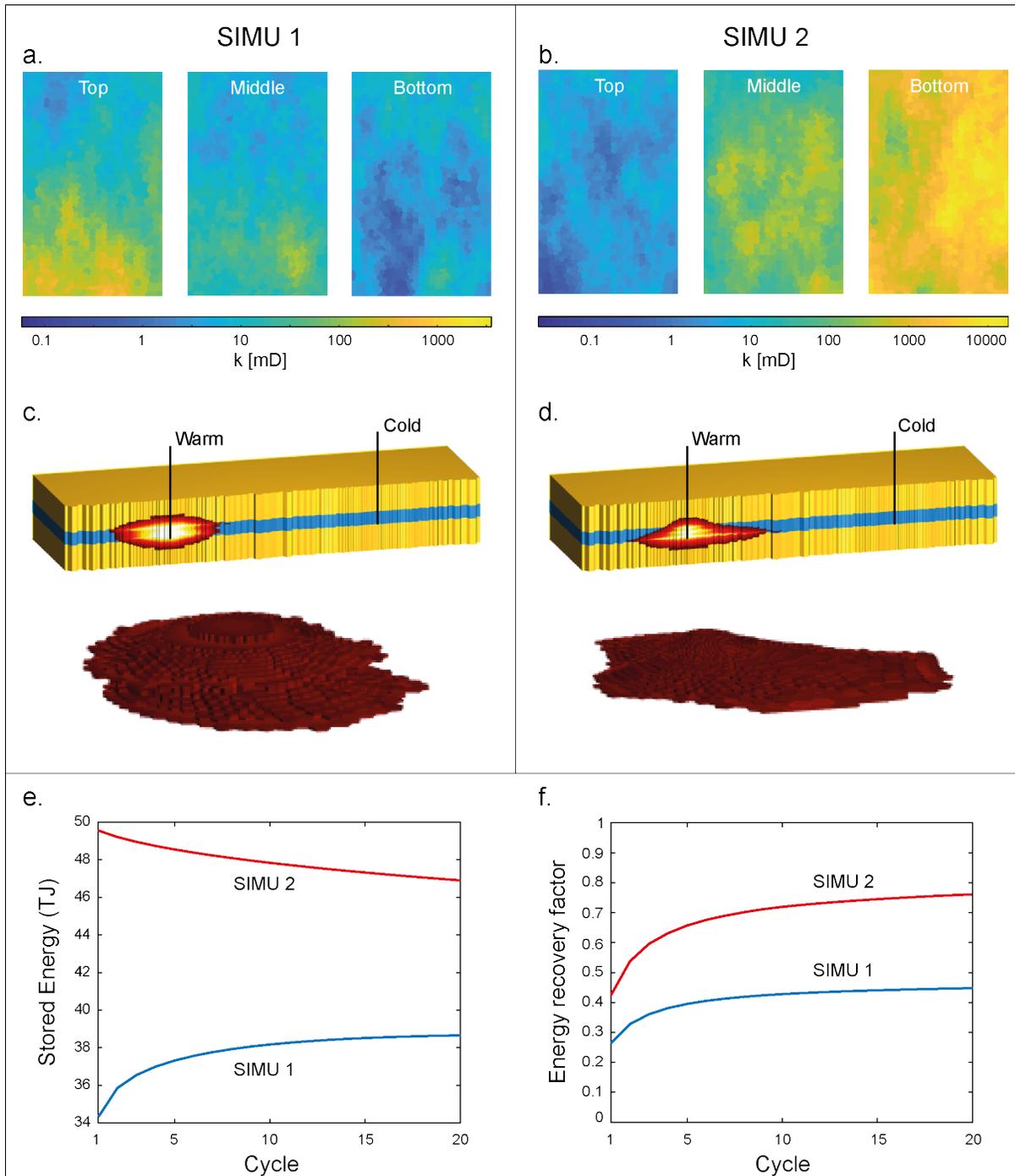


Figure 12: **a,b** Permeability distribution at the top, middle and bottom of the aquifers. Logarithmic scale. **c,d** Cross section of the model and extracted plume at the beginning of the unloading phase for the 10<sup>th</sup> cycle **e.** Evolution of the injected energy during the HT-ATES exploitation. **f.** Evolution of the energy recovery factor during the HT-ATES exploitation.

712 could further be investigated in numerical models when fully assessing the HT-ATES performance and  
713 its environmental impact. It is currently not possible to conclude on the aquifer flow velocity from  
714 the available discharge rates measured at the wells in the GGB. Further investigations are required as  
715 velocities larger than 15-20 m a<sup>-1</sup> have a considerable impact on the HT-ATES thermal recovery (Fig. 8).  
716 For large aquifer velocities (>50 m a<sup>-1</sup>), storage is not ideal but several strategic options can be taken.  
717 If the velocity drift is sufficiently high, the stored energy could be recovered at a second well. In this  
718 case, one well will always operate in an injection mode and the other in a production mode. Bloemendal  
719 and Olsthoorn (2018) also suggested to use multiple pairs of warm and cold wells. Another option is to  
720 place the wells ideally close to a structural trap (e.g. sealed fault) that confines the warm water during  
721 the storage period.

722 Finally, we have employed in our study the same well schedule over 20 years, considering constant energy  
723 availability and demands. In reality, this is unlikely to be the case and the loading-unloading phases  
724 should be adapted to the true energetic needs and available sources of heat. Integrating the energy  
725 demands with meteorological data over a longer period and considering up-to-date energy policy and  
726 technical advances will help forecasting the future needs and demands for the Canton of Geneva and  
727 further constrain the HT-ATES performance.

## 728 6 Conclusions

729 Our new *geothermal* module in MRST allows for intuitive and rapid testing of HT-ATES strategies  
730 involving complex injection schedules, as well as for various geothermal applications. MRST is an open-  
731 source software released under the GPL 3 license, where the source code for all parts of the simulator can  
732 be modified easily. While a number of compiled, third-generation language implementations of similar  
733 functionality exists, high-quality C++ or Fortran implementations require a large amount of domain-  
734 specific knowledge from users who wish to modify the inner workings of the simulator. We hope that a  
735 implementation in a high-level, fourth-generation language will be more widely accessible to users who  
736 wish to write their own simulators.

737 The results of our study allow us to decipher the relative importance of some of the investigated param-  
738 eters and their control on thermal recovery efficiency and shows that the performance of the HT-ATES  
739 will not be affected by the salinity nor by aquifer velocities lower than 15 m a<sup>-1</sup>. Typical salinities encoun-  
740 tered in the first 2 km of sedimentary basins or aquifer flow velocities lower than 15 m a<sup>-1</sup> do not affect  
741 the thermal recovery. Porosity changes if not linked to permeability will also not affect the HT-ATES  
742 performance. Thermal losses by conduction, and thus thermal recovery, can no longer be derived from  
743 the aspect ratio of the stored warm water when bhp limits control the injected/produced volumes. The  
744 effects of bhp limits on the injected/produced volumes, and subsequent thermal recovery are even more

745 pronounced in heterogeneous aquifers if the wells are not placed carefully. Moreover, for such aquifers  
746 the shape of the stored volumes of warm water and its impact on thermal recovery are hard to predict.  
747 High-permeability and fairly homogeneous aquifers represent interesting targets for seasonal HT-ATES  
748 systems because they can store large amount of heat in a limited time-window. On the other hand, they  
749 also favour thermal losses by free convection, and thus limit the thermal recovery. Our results show that  
750 for aquifer permeabilities below 500 mD, thermal losses by convection are strongly reduced, even absent  
751 in some cases, and the thermal recovery factor reaches up to 0.9. These aquifers, however, have limited  
752 seasonal storage volume, as the injection and production rates are scaled with the permeability to avoid  
753 rock fracturing.

754 This study highlights the importance of thorough numerical simulations to evaluate the thermal per-  
755 formance of an HT-ATES system in more realistic exploitation conditions before its realisation. Its  
756 optimisation can only be achieved through a global energy policy at the county scale that promotes the  
757 development of renewable energies, low-energetic heating facilities and constrained forecasts of the future  
758 energetic demands. For the specific case of the Chenevier plant, near Geneva, two approaches can be  
759 undertaken to exploit the  $\sim 35$  GWh in excess of heat. The first is to apply a cut-off temperature during  
760 the unloading phases and stop extracting the warm water when its temperature drops below  $80^\circ\text{C}$ . The  
761 energy recovery factor is expected to be low in the first cycles but to improve considerably with time  
762 and reach 0.8. The aquifer will, however, significantly warm up, which can have a strong impact on the  
763 environment. The second approach is to keep a volume recovery factor close to one but only inject in  
764 the district heating networks the water at a temperature higher than  $80^\circ\text{C}$ . The environmental impact  
765 is limited but the energy recovery factor generally remains below 0.5. This can be improved if the ex-  
766 tracted water is exploited at lower temperatures, either by optimisation of the existing networks or by  
767 diversification of the economical applications. The Molasse aquifers are economically more viable than  
768 the Malm aquifers for storage up to  $90^\circ\text{C}$  because of their lower drilling costs for comparable energy  
769 recovery factors. The thermal perturbations in these aquifers are non-negligible, which means that the  
770 volume of injected water must be controlled to comply with the environmental regulations in Switzer-  
771 land. The Malm aquifers become, however, interesting for heat storage above  $90^\circ\text{C}$  because of their  
772 limited environmental impact. More in-situ data are required to characterise the spatial variations of the  
773 aquifer properties in the Geneva Canton to provide a more detailed assessment of the economical and  
774 environmental impacts of heat storage. Thermo-mechanical and thermo-chemical processes should also  
775 be integrated in further modelling study. Nevertheless, the methodology and approach presented in this  
776 study can be applied to other heterogeneous aquifers of the Molasse Basin and more generally in foreland  
777 basins, where such type of isolated and spatially limited reservoirs are commonly found.

## 7 Acknowledgment

M. Collignon and M. Alcanié were funded by GENERATE, SNF project (PYAPP2.66900, PI Matteo Lupi). M. Lupi is a SCCER-SoE Professor supported by KTI funding. Ø. S. Klemetsdal was supported by the Research Council of Norway under grant no. 244361. O. Møyner was funded by VISTA, which is a basic research programme funded by Equinor and conducted in close collaboration with The Norwegian Academy of Science and Letters. The authors would like to thank the SIG (Services Industriels de Genève), and in particular Michel Meyer and Loic Quiquerez, for providing internal reports and the data for Figure 2, as well as Thomas Driesner for providing a table with computed parameters (i.e. fluid density, viscosity, enthalpy and heat capacity). The authors also thank Nicole Lupi, Knut-Andreas Lie and Luca Guglielmetti for fruitful discussions. Finally, two anonymous reviewers and the Editor, Christopher Bromley, are thanked for their comments on a previous version of the manuscript.

## References

- Amberger, G.  
1978. Contribution à l'étude du quaternaire de la région lémanique: Résultats de quelques sondages profonds exécutés à genève. Eclogae Geologicae Helvetiae, 71:193–206.
- Andersson, O.  
2007. Aquifer thermal energy storage (ates). In Thermal Energy Storage for Sustainable Energy Consumption. NATO Science Series (Mathematics, Physics and Chemistry)., H. Paksoy, ed., volume 234, Pp. 155–176. Dordrecht: Springer.
- Baujard, C., S. Signorelli, T. Kohl, and S. G. Kommission  
2007. Atlas des ressources géothermiques de la Suisse occidentale: domaine Sud-Ouest du Plateau Suisse, Contribution à la géologie de la Suisse. Géophysique. Commission Suisse de Géophysique.
- Becker, D., G. Rauber, and L. Scherler  
2013. New small mammal fauna of late middle eocene age from a fissure filling at la verrerie de roches (jura, nw switzerland). Revue de Paléobiologie, 32:433–446.
- Berge, R. L., Ø. S. Klemetsdal, and K.-A. Lie  
2018. Unstructured voronoi grids conforming to lower dimensional objects. Comput. Geosci. In press.
- Biot, M.  
1941. General theory of three-dimensional consolidation. Journal of Applied Physics, 12:155–164.
- Bloemendal, M. and N. Hartog  
2018. Analysis of the impact of storage conditions on the thermal recovery efficiency of low-temperature ates systems. Geothermics, 71:306–319.

810 Bloemendal, M., M. Jaxa-Rozen, and T. Olsthoorn  
811 2018. Methods for planning of ates systems. Applied Energy, 216:534–557.

812 Bloemendal, M. and T. Olsthoorn  
813 2018. Ates systems in aquifers with high ambient groundwater flow velocity. Geothermics, 75:81–92.

814 Bloemendal, M., T. Olsthoorn, and F. Boons  
815 2014. How to achieve optimal and sustainable use of the subsurface for aquifer thermal energy storage. Energy  
816 Policy, 66:104–114.

817 Blondel, T.  
818 1990. Lithostratigraphie synthétique du jurassique et du crétaé inférieur de la partie septentrionale de la  
819 montagne du vuache. Archives des Sciences, Genève, 43:175–191.

820 Bonte, M., B. M. van Breukelen, and P. J. Stuyfzand  
821 2013. Temperature-induced impacts on groundwater quality and arsenic mobility in anoxic aquifer sediments  
822 used for both drinking water and shallow geothermal energy production. Water Research, 47:5088–5100.

823 Brentini, M.  
824 2018. Impact d’une donnée géologique hétérogène dans la gestion des géo-ressources: analyse intégrée et  
825 valorisation de la stratigraphie à travers le bassin genevois (Suisse, France). PhD thesis.

826 Brons, H., J. Griffioen, C. Appelo, and A. Zehnder  
827 1991. (bio)geochemical reactions in aquifer material from a thermal energy storage site. Water Research,  
828 25:729–736.

829 Buscheck, T. A., J. M. Bielicki, and J. B. Randolph  
830 2017. CO<sub>2</sub> earth storage: Enhanced geothermal energy and water recovery and energy storage. Energy Procedia,  
831 114:6870–6879.

832 CH-GSchV  
833 1998. Gewässerschutzverordnung vom 28. Oktober 1998 (Water Protection Order). Schweizer Bundesrat.

834 Charollais, J.-J., M. Weidmann, J.-P. Berger, B. Engesser, J.-F. Hotellier, G. Gorin, B. Reichenbacher, and  
835 P. Schäfer  
836 2007. La molasse du bassin franco-genevois et son substratum. Archives des Sciences, 60:59–174.

837 Charollais, J.-J., R. Wernli, B. Mastrangelo, J. Metzger, R. Busnardo, B. Clavel, M. Conrad, E. Davaud,  
838 B. Granier, M. Saint Martin, and M. Weidmann  
839 2013. Présentation d’une nouvelle carte géologique du vuache et du mont de musières (haute-savoie, france).  
840 Archives des Sciences, 66:1–64.

841 Chelle-Michou, C., D. D. Couto, A. Moscariello, P. Renard, and E. Rusillon  
842 2017. Geothermal state of the deep western alpine molasse basin, france-switzerland. Geothermics, 67:48–65.

843 Chevalier, G., L. W. Diamond, and W. Leu  
844 2010. Potential for deep geological sequestration of CO<sub>2</sub> in Switzerland: a first appraisal. Swiss Journal of  
845 Geosciences, 103:427–455.

846 Choffat, M.  
847 1878. Sur le callovien et l'oxfordien dans le Jura. Bulletin de la société géologique de France, 6:358–364.

848 Collignon, M., A. Mazzini, D. W. Schmid, and M. Lupi  
849 2018a. Modelling fluid flow in active piercements: Challenge and approaches. Marine and Petroleum Geology,  
850 90:157–172.

851 Collignon, M., D. W. Schmid, C. Galerne, M. Lupi, and A. Mazzini  
852 2018b. Modelling fluid flow in clastic eruptions: Application to the Lusi mud eruption. Marine and Petroleum  
853 Geology, 90:173–190.

854 Colombo, U.  
855 1992. Development and the global environment. In The energy-environment connection, J. Hollander, ed.,  
856 Pp. 3–14. Washington, D.C.: Island Press.

857 Conrad, M.-A.  
858 1969. Les calcaires urgoniens dans la région entourant Genève. Eclogae Geologicae Helvetiae, 62:1–79.

859 Courtois, N., J.-P. Marchal, A. Menjoz, P. Monnot, Y. Noël, V. Petit, D. Thiéry, A. Grisey, and D. Grasselly  
860 2006. Application du stockage thermique en aquifère au chauffage et au refroidissement de serres maraîchères  
861 en France: étude de préféabilité. BRGM.

862 Dickinson, J., N. Buik, M. Matthews, and A. Snijders  
863 2009. Aquifer thermal energy storage: theoretical and operational analysis. Géotechnique, 59:249–260.

864 Diesler, C.  
865 1914. Stratigraphie und Tektonik des Rotliegenden und der Trias beiderseits des Rheins zwischen Rheinfelden  
866 und Augst. PhD thesis.

867 Dincer, I.  
868 1998. Energy and environmental impacts: Present and future perspectives. Energy Sources, 20:427–453.

869 Dincer, I.  
870 2000. Renewable energy and sustainable development: a crucial review. Renewable and Sustainable Energy  
871 Reviews, 4:157–175.

872 Dincer, I. and M. A. Rosen  
873 2011. Thermal Energy Storage: Systems and Applications. Wiley.

874 Doughty, C., G. Hellström, and C. F. Tsang  
875 1982. A dimensionless parameter approach to the thermal behavior of an aquifer thermal energy storage system.  
876 Water Resources Research, 18:571–587.

877 Driesner, T.  
878 2007. The system  $\text{H}_2\text{O}-\text{NaCl}$  ii. correlations for molar volume, enthalpy, and isobaric heat capacity from 0 to  
879 1000 degrees c, 1 to 5000 bar, and 0 to 1  $\text{x}_{\text{NaCl}}$ . Geochimica et Cosmochimica Acta, 71:4902–4919.

880 Drijver, B.  
881 2011. High temperature aquifer thermal energy storage (ht-ates): Water treatment in practice. In 1<sup>e</sup> Nationaal  
882 Congres Bodemenergie, Utrecht, Nederland, 13-14 Oktober 2011.

883 Drijver, B., M. V. Aarssen, and B. de Zwart  
884 2012. High-temperature aquifer thermal energy storage (ht-ates): sustainable and multi-usable. In Innostonk  
885 2012. 12<sup>th</sup> International Conference on Energy Storage.

886 Faessler, J., B. M. Lachal, L. Quiquerez, and S. S. I. de Genève  
887 2015. Géothermie de moyenne profondeur: Scénarios d'utilisation de la ressource via des réseaux de chauffage  
888 à distance - Enjeux et principaux enseignements. Genève: Services Industriels de Genève.

889 Fleuchaus, P., B. Godschalk, I. Stober, and P. Blum  
890 2018. Worldwide application of aquifer thermal energy storage - a review. Renewable and Sustainable Reviews,  
891 94:861–876.

892 GeoMolTeam  
893 2015. GeoMol - Assessing subsurface potentials of the Alpine Foreland Basins for sustainable planning and use  
894 of natural resources. Bayerisches Landesamt für Umwelt.

895 Hähnlein, S., P. Bayer, and P. Blum  
896 2010. International legal status of the use of shallow geothermal energy. Renewable and Sustainable Energy  
897 Reviews, 14:2611–2625.

898 Hähnlein, S., P. Bayer, G. Ferguson, and P. Blum  
899 2013. Sustainability and policy for the thermal use of shallow geothermal energy. Energy Policy, 59:914–925.

900 Hartog, N., B. Drijver, I. Dinkla, and M. Bonte  
901 2013. Field assessment of the impacts of aquifer thermal energy storage (ates) systems on chemical and microbial  
902 groundwater composition. In Proceeding of the European Geothermal conference. Pisa, Italy.

903 HeatStore  
904 . Geothermica – era net cofund heatstore (project n.170153-4401).

905 Hellström, G., C. Tsang, and J. Claesson  
906 1979. Heat storage in aquifers: buoyancy flow and thermal stratification problems.

907 Hooker, J. and M. Weidmann  
908 2007. A diverse rodent fauna from the middle bartonian (eocene) of les alleveys, switzerland: snapshot of the  
909 early theridomyid radiation. Swiss Journal of Geosciences, 100:469–493.

910 Jenne, E., O. Andersson, and A. Willemsen  
911 1992. Well, hydrology and geochemistry problems encountered in ates systems and their solutions.

912 Jesuβek, A., S. Grandel, and A. Dahmke  
913 2012. Impacts of subsurface heat storage on aquifer hydrogeochemistry. Energy, 69:1999–2012.

914 Kappelmeyer, O. and R. Haenel  
915 1974. Geothermics with special reference to application. Stuttgart, Germany: Schweizerbart Science Publishers.

916 Kim, J., W. Yoon, J. Jeon, M. Koo, and Y. Keehm  
917 2010. Numerical modeling of aquifer thermal energy storage system. Energy, 35:4955–4965.

918 Krogstad, S., K.-A. Lie, O. Møyner, H. M. Nilsen, X. Raynaud, and B. Skaflestad  
919 2015. Mrst-ad—an open-source framework for rapid prototyping and evaluation of reservoir simulation problems.  
920 In SPE reservoir simulation symposium. Society of Petroleum Engineers.

921 Kuhlemann, J. and O. Kempf  
922 2002. Post-eocene evolution of the north alpine foreland basin and its response to alpine tectonics. Sedimentary  
923 Geology, 152:45–78.

924 Leamon, G. R.  
925 2006. Petroleum well costs. Master’s thesis, School of Petroleum Engineering, The University of New South  
926 Wales, Sydney, N.S.W., Australia.

927 Lee, K. S.  
928 2010. A review on concepts, applications, and models of aquifer thermal energy storage systems. Energies,  
929 3:1320–1334.

930 Lie, K.-A.  
931 2019. An Introduction to Reservoir Simulation Using MATLAB/GNU Octave: User guide for the  
932 MATLAB Reservoir Simulation Toolbox (MRST). Cambridge University Press.

933 Lie, K.-A., S. Krogstad, I. S. Ligaarden, J. R. Natvig, H. M. Nilsen, and B. Skaflestad  
934 2012. Open source MATLAB implementation of consistent discretisations on complex grids. Comput. Geosci.,  
935 16:297–322.

936 Lund, H., P. A. Østergaard, M. Chang, S. Werner, S. Svendsen, P. Sorknæs, J. E. Thorsen, F. Hvelplund, B. O. G.  
937 Mortensen, B. V. Mathiesen, C. Bojesen, N. Duic, X. Zhang, and B. Møller  
938 2018. The status of 4<sup>th</sup> generation district heating: Research and results. Energy, 164:147–159.

939 Lund, H., S. Werner, R. Wiltshire, S. Svendsen, J. E. Thorsen, F. Hvelplund, and B. V. Mathiesen  
940 2014. 4<sup>th</sup> generation district heating (4gdh). integrating smart thermal grids into future sustainable energy  
941 systems. Energy, 68:1–11.

942 Makhloufi, Y., E. Rusillon, M. Brentini, A. Moscariello, M. Meyer, and E. Samankassou  
943 2018. Dolomitization of the upper jurassic carbonate rocks in the geneva basin, switzerland and france. Swiss  
944 Journal of Geosciences.

945 McCann, T., C. Pascal, M. Timmerman, P. Krzywiec, J. López-Gómez, L. Wetzel, C. Krawczyk, H. Rieke, and

946 J. Lamarche  
947 2006. Post-variscan (end carboniferous-early permian) basin evolution in western and central europe. Geological  
948 Society London Memoirs, 35:355–388.

949 Molz, F., J. Melville, O. Güven, and A. Parr  
950 1983a. Aquifer thermal energy storage: An attempt to counter free thermal convection. Water Resources  
951 Research, 19:922–930.

952 Molz, F., J. Melville, A. Parr, D. King, and M. Hopf  
953 1983b. Aquifer thermal energy storage: A well doublet experiment at increased temperatures. Water Resources  
954 Research, 19:149–160.

955 Molz, F., A. Parr, P. Andersen, and V. Lucido  
956 1979. Thermal energy storage in a confined aquifer: Experimental result. Water Resources Research, 15:1509–  
957 1514.

958 Moscariello, A., A. Pugin, W. Wildi, C. Beck, E. Chapron, M. De Batist, S. Girardclos, S. Ivy Ochs, A.-M.  
959 Rachoud-Schneider, and C. Signer  
960 1998. Déglaçiation würmienne dans des conditions lacustres à la terminaison occidentale du bassin lémanique  
961 (suisse occidentale et france). Eclogae Geologicae Helvetiae, 91:185–201.

962 OFEV  
963 2009. Exploitation de la chaleur tirée du sol et du sous-sol. Office fédéral de l'environnement OFEV.

964 O'Sullivan, M. J., K. Pruess, and M. J. Lippmann  
965 2000. Geothermal reservoir simulation: the state-of-practice and emerging trends. In Proceeding World  
966 Geothermal Congress 2000.

967 PGG  
968 2011. Evaluation du potentiel géothermique du canton de Genève. Etat de Genève.

969 Platt, N. H. and B. Keller  
970 1992. Distal alluvial deposits in a foreland basin setting - the lower freshwater molasse (lower miocene),  
971 switzerland: sedimentology, architecture and palaeosols. Sedimentology, 39:545–565.

972 Possemiers, M., M. Huysmans, and O. Batelaan  
973 2014. Influence of aquifer thermal energy storage on groundwater quality: A review illustrated by seven case  
974 studies from belgium. Journal of Hydrology: Regional Studies, 2:20–34.

975 Pruess, K., C. Oldenburg, and G. Moridis  
976 1999. TOUGH2 User's Guide, Version 2.0. Lawrence Berkeley National Laboratory.

977 Quiquerez, L.  
978 2017. Décarboner le système énergétique à l'aide des réseaux de chaleur: état des lieux et scénarios propectifs  
979 pour le canton de Genève. PhD thesis.

980 Quiquerez, L., J. Faessler, M. Bernard, and S. I. de Genève  
981 2015. Réseaux thermiques multi-ressources efficients et renouvelables: Etude de cas de la connexion des réseaux  
982 thermiques CADIOM (chaleur fatale) et CADSIG (gaz) à Genève et perspectives d'évolution. Genève: Services  
983 Industriels de Genève.

984 Quiquerez, L., J. Faessler, and B. M. Lachal  
985 2016. Valorisation de la chaleur renouvelable et des rejets thermiques: bilan et enjeux de l'interconnexion des  
986 deux plus grands réseaux thermiques genevois. Bulletin de l'ARPEA, 269:25–31.

987 Ramsay, J. G.  
988 1963. Stratigraphy, structure and metamorphism in the western alps. Proceedings of the Geologists' Association,  
989 74:357–390.

990 Rusillon, E.  
991 2017. Characterisation and rock typing of deep geothermal reservoirs in the Greater Geneva Basin (Switzerland  
992 & France. PhD thesis.

993 Rybach, L.  
994 1992. Geothermal potential of the swiss molasse basin. Eclogae Geologicae Helvetiae, 85:733–744.

995 Sanner, B.  
996 1999. High temperature underground thermal energy storage. state-of-the-art and prospects.

997 Schüppler, S., P. Fleuchaus, and P. Blum  
998 2019. Techno-economic and environmental analysis of an aquifer thermal energy storage (ates) in germany.  
999 Geothermal Energy, 7:11:24.

1000 Signer, C. and G. E. Gorin  
1001 1995. New geological observations between the jura and the alps in the geneva area, as derived from reflection  
1002 seismic data. Eclogae Geologicae Helvetiae, 88:235–265.

1003 Signorelli, S., N. Andenmatten Berthoud, and T. Kohl  
1004 2004. Geothermischer Ressourcenatlas der Schweiz. Erarbeitung und Bewertung des geothermischen Potentials  
1005 der Schweiz. Bundesamts für Energie BFE.

1006 Sommaruga, A.  
1007 1997. Geology of the Central Jura and the Molasse Basin: new insight into an evaporite-based foreland fold  
1008 and thrust belt. PhD thesis.

1009 Sommaruga, A.  
1010 1999. Décollement tectonics in the jura foreland fold-and-thrust belt. Marine and Petroleum Geology, 16:111–  
1011 134.

1012 Sommer, W., J. Valstar, P. V. Gaans, and H. Rijnaarts  
1013 2013. The impact of aquifer heterogeneity on the performance of aquifer thermal energy storage. Water  
1014 Resources Research, 49:8128–8138.

- 1015 Sommer, W., J. Valstar, I. Leusbrock, T. Grotenhuis, and H. Rijnaarts  
1016 2015. Optimization and spatial pattern of large-scale aquifer thermal energy storage. Applied Energy, 137:322–  
1017 337.
- 1018 Sowers, L., K. York, and L. Stiles  
1019 2006. Impact of the thermal build up on groundwater chemistry and aquifer microbes. In Proceedings of  
1020 Ecostock, Pomena, 31<sup>th</sup> May - 2<sup>nd</sup> June, Pp. 1–7.
- 1021 Spivey, J., W. McCain, and R. North  
1022 2004. Estimating density, formation volume factor, compressibility, methane solubility, and viscosity for oilfield  
1023 brines at temperatures from 0 to 275°C, pressures to 200 mpa, and salinities to 5.7 mole/kg. Journal of Canadian  
1024 Petroleum Technology.
- 1025 Trümpy, R.  
1026 1980. Geology of Switzerland - a guide-book. Part A: An outline of the geology of Switzerland. Part B:  
1027 Geological excursions. Wepf and Co.
- 1028 Van Lopik, J. H., N. Hartog, and W. J. Zaadnoordijk  
1029 2016. The use of salinity contrast for density difference compensation to improve the thermal recovery efficiency  
1030 in high-temperature aquifer thermal energy storage systems. Hydrogeol J., 24:1255–1271.
- 1031 Wilson, M., E. Neumann, G. Davies, M. Timmerman, M. Heeremans, and B. Larsen  
1032 2004. Permo-carboniferous magmatism and rifting in europe: introduction. Geological Society London Special  
1033 Publications, 223:1–10.
- 1034 Winterleitner, G., F. Schütz, C. Wenzlaff, and E. Huenges  
1035 2018. The impact of reservoir heterogeneities on high-temperature aquifer thermal energy storage systems. a  
1036 case study from northern oman. Geothermics, 74:150–162.